

# Bulletin of Volcanology

## Experimental Sintering of Ash at Conduit Conditions and Implications for the Longevity of Tuffisites --Manuscript Draft--

<b>Manuscript Number:</b>					
<b>Full Title:</b>	Experimental Sintering of Ash at Conduit Conditions and Implications for the Longevity of Tuffisites				
<b>Article Type:</b>	Research Article				
<b>Corresponding Author:</b>	James E. Gardner Jackson School of Geosciences Austin, TX UNITED STATES				
<b>Corresponding Author Secondary Information:</b>					
<b>Order of Authors:</b>	James E. Gardner Fabian Wadsworth Edward Llewellyn James Watkins Jason Coumans				
<b>Funding Information:</b>	<table border="1"> <tr> <td>National Science Foundation (EAR-1348050)</td> <td>Dr. James E. Gardner</td> </tr> <tr> <td>UK Natural Environmental Research Council (NE/N002954/1)</td> <td>Dr. Edward Llewellyn</td> </tr> </table>	National Science Foundation (EAR-1348050)	Dr. James E. Gardner	UK Natural Environmental Research Council (NE/N002954/1)	Dr. Edward Llewellyn
National Science Foundation (EAR-1348050)	Dr. James E. Gardner				
UK Natural Environmental Research Council (NE/N002954/1)	Dr. Edward Llewellyn				
<b>Abstract:</b>	<p>Escape of gas from magma in the conduit plays a crucial role in mitigating explosivity. Tuffisite veins - ash-filled cracks that form in and around volcanic conduits - represent important gas escape pathways. Sintering of the ash infill decreases its porosity, eventually forming dense glass that is impermeable to gas. We present an experimental investigation of surface-tension driven sintering and associated densification of rhyolitic ash under shallow conduit conditions. Suites of isothermal (700-800°C) and isobaric H<sub>2</sub>O pressure (20 and 40 MPa) experiments were run for durations of 5-90 minutes. Obsidian powders with two different size distributions were used: 1-1600 μm (mean size = 89 μm); and 63-400 μm (mean size = 185 μm). All samples evolved similarly through four textural phases: Phase 1) loose and cohesionless particles; Phase 2) particles sintered at contacts and surrounded by fully-connected tortuous pore space of up to ~40% porosity; Phase 3) continuous matrix of partially coalesced particles that contains both isolated spherical vesicles and connected networks of larger, contorted vesicles; Phase 4) dense glass with 2-5% fully-isolated vesicles that are mainly spherical. Textures evolve faster at higher temperature and higher H<sub>2</sub>O pressure. Coarse samples sinter more slowly, and contain fewer, larger vesicles when fully sintered. We quantify the sintering progress by measuring porosity as a function of experimental run-time, and find an excellent collapse of data when run-time is normalized by the sintering timescale <math>\lambda_s = (\eta R/\sigma)</math>, where <math>\eta</math> is melt viscosity, R is mean particle radius, and <math>\sigma</math> is melt-gas surface tension. Because timescales of diffusive H<sub>2</sub>O equilibration are generally fast compared to those of sintering, the relevant melt viscosity is calculated from the solubility H<sub>2</sub>O content at experimental temperature and pressure. We use our results to develop a framework for estimating ash sintering rates under shallow conduit conditions, and predict that sintering of ash to dense glass can seal tuffisites in minutes to hours, depending on pressure (i.e., depth), temperature, and ash size.</p>				
<b>Suggested Reviewers:</b>	<p>Jonathan Castro castroj@uni-mainz.de Jon Castro is a leading expert on tuffisite formation and textures.</p> <p>Hugh Tuffen h.tuffen@lancaster.ac.uk</p>				

High Tuffen is a leading expert on the natural occurrence and textures of tuffisite veins.

Michael Manga

[manga@seismo.berkeley.edu](mailto:manga@seismo.berkeley.edu)

Michael Manga has extensive knowledge and experience in modeling of volcanic degassing

[Click here to view linked References](#)

1 **Experimental Sintering of Ash at Conduit Conditions and Implications for the**  
2 **Longevity of Tuffisites**

3

4 James E. Gardner<sup>a,\*</sup>, Fabian B. Wadsworth<sup>b</sup>, Edward W. Llewelin<sup>c</sup>,

5 James M. Watkins<sup>d</sup>, and Jason P. Coumans<sup>c</sup>

6

7

8 *<sup>a</sup>Department of Geological Sciences, Jackson School of Geosciences, The University of Texas at*  
9 *Austin, Austin, TX, 78712-0254, U.S.A.*

10 *<sup>b</sup>Earth and Environmental Sciences, Ludwig-Maximilians-Universität, Theresienstr. 41/III,*  
11 *80333 München, Germany*

12 *<sup>c</sup>Department of Earth Sciences, Durham University, Durham, DH1 3LE, U.K.*

13 *<sup>d</sup>Department of Geological Earth Sciences, University of Oregon, Eugene, OR, 97403-1272,*  
14 *U.S.A.*

15

16

17 <sup>\*</sup>Corresponding author. Fax: +1 512 471 9425

18 E-mail address: [gardner@mail.utexas.edu](mailto:gardner@mail.utexas.edu) (J.E. Gardner)

19 **Abstract**

20 Escape of gas from magma in the conduit plays a crucial role in mitigating explosivity. Tuffisite  
21 veins – ash-filled cracks that form in and around volcanic conduits – represent important gas  
22 escape pathways. Sintering of the ash infill decreases its porosity, eventually forming dense glass  
23 that is impermeable to gas. We present an experimental investigation of surface-tension driven  
24 sintering and associated densification of rhyolitic ash under shallow conduit conditions. Suites of  
25 isothermal (700–800°C) and isobaric H<sub>2</sub>O pressure (20 and 40 MPa) experiments were run for  
26 durations of 5–90 minutes. Obsidian powders with two different size distributions were used: 1–  
27 1600 μm (mean size = 89 μm); and 63–400 μm (mean size = 185 μm). All samples evolved  
28 similarly through four textural phases: Phase 1) loose and cohesion-less particles; Phase 2)  
29 particles sintered at contacts and surrounded by fully-connected tortuous pore space of up to  
30 ~40% porosity; Phase 3) continuous matrix of partially coalesced particles that contains both  
31 isolated spherical vesicles and connected networks of larger, contorted vesicles; Phase 4) dense  
32 glass with 2–5% fully-isolated vesicles that are mainly spherical. Textures evolve faster at higher  
33 temperature and higher H<sub>2</sub>O pressure. Coarse samples sinter more slowly, and contain fewer,  
34 larger vesicles when fully sintered. We quantify the sintering progress by measuring porosity as  
35 a function of experimental run-time, and find an excellent collapse of data when run-time is  
36 normalized by the sintering timescale  $\lambda_s = \frac{\eta \bar{R}}{\sigma}$ , where  $\eta$  is melt viscosity,  $\bar{R}$  is mean particle  
37 radius, and  $\sigma$  is melt–gas surface tension. Because timescales of diffusive H<sub>2</sub>O equilibration are  
38 generally fast compared to those of sintering, the relevant melt viscosity is calculated from the  
39 solubility H<sub>2</sub>O content at experimental temperature and pressure. We use our results to develop a  
40 framework for estimating ash sintering rates under shallow conduit conditions, and predict that

41 sintering of ash to dense glass can seal tuffisites in minutes to hours, depending on pressure (i.e.,  
42 depth), temperature, and ash size.

43

44 Keywords: sinter; ash; tuffisite; permeability; diffusion; hydration

## 45 **Introduction**

46 Volcanic eruptions often fluctuate between highly explosive emission of ash and pumice, and  
47 effusion of lava, all while erupting the same gas-charged magma (Eichelberger et al., 1986;  
48 Castro et al., 2012; Schipper et al., 2013). The transition to effusive behavior is thought to result  
49 from the escape of magmatic gases, suppressing fragmentation (Eichelberger et al., 1986; Jaupart  
50 and Allegre, 1991). One mechanism by which gases can escape is magma fracturing in response  
51 to shear-induced deformation during ascent (Gonnermann and Manga, 2003). Tuffisite veins –  
52 ash-filled cracks found in lava flows, volcanic conduits, and Vulcanian blocks – are thought to  
53 be remnants of magma fracturing (Stasiuk et al., 1996; Tuffen et al., 2003; Castro et al., 2012).

54 The efficiency of magma degassing through fractures depends in part on the spacing of  
55 fractures and timescale over which the fractures remain open and permeable (Cabrera et al.,  
56 2011; Berlo et al., 2013; Castro et al., 2014; Saubin et al., 2016). Diffusive modeling of remnant  
57 H<sub>2</sub>O concentration gradients next to tuffisites suggests that fractures remain open to gas escape  
58 for minutes to tens of hours, depending on the assumed temperature (Cabrera et al., 2011; Castro  
59 et al., 2012; Berlo et al., 2013; von Aulock et al., 2013; Saubin et al., 2016). These veins are  
60 usually filled with a matrix of juvenile ash, interspersed with vesicular clasts and lithic rock  
61 fragments (Tuffen and Dingwell, 2005). Deposition of ash in a fracture can clog it and reduce its  
62 permeability (Tuffen et al., 2003; Tuffen and Dingwell, 2005). Tuffisite veins are often partially  
63 to densely welded, with very low vesicularities (Tuffen et al., 2003; Castro et al., 2014; Saubin et  
64 al., 2016), indicating that the ash within them has sintered (Wadsworth et al., 2016a,b). Sintering  
65 decreases vesicularity and permeability of the particle pack, and occurs when viscous particles  
66 that share contacts undergo time-dependent coalescence driven by the interfacial tension between  
67 the particles and the ambient fluid in the interstitial pore space (Wadsworth et al., 2014, 2016b).

68 Consequently, the time span over which gas can pass through fractures will depend partly on  
69 how quickly ash sinters. Shear stresses acting on the particle–particle contacts may accelerate  
70 sintering in bulk compaction processes (Michaut et al., 2009; Quane et al., 2009).

71 Experimental studies have investigated sintering of soda-lime-silica glass beads (Wadsworth  
72 et al., 2014, 2016b), synthetic angular glass shards (Vasseur et al. 2013; Wadsworth et al., 2014),  
73 and natural tuffisite material (Kendrick et al., 2016). These studies show that melt viscosity and  
74 grain size of the starting particle population are important controls on the timescale of sintering.  
75 Wadsworth et al. (2016b) found that the characteristic sintering timescale  $\lambda_s$  (s) for randomly  
76 packed, monodisperse spherical particles (droplets when molten) is given by

77

$$\lambda_s = \frac{\eta L}{\sigma} \quad (1)$$

78

79 where  $\eta$  is droplet viscosity (Pa s),  $\sigma$  is surface tension (N m<sup>-1</sup>), and  $L$  (m) is a characteristic  
80 length scale, which is the particle radius, in the case of incipient sintering, or inter-particle pore  
81 radius, in the case of thorough sintering.

82 All of the experiments referenced above were run at atmospheric pressure, but dissolved H<sub>2</sub>O  
83 contents indicate that natural tuffisites can form and seal at vapor pressures >8 MPa (e.g., Castro  
84 et al., 2014; Saubin et al., 2016). Importantly, ash in fractures at depth is likely to be relatively  
85 rich in H<sub>2</sub>O, because H<sub>2</sub>O solubility increases with fluid pressure (Blank et al., 1993; Liu et al.,  
86 2005), and, in turn, H<sub>2</sub>O dissolved in silicate melt strongly lowers viscosity (Hess and Dingwell,  
87 1996), implying (from Eqn. 1) that  $\lambda_s$  is substantially shorter at depth. The efficiency of  
88 degassing via fractures could thus decrease with depth within the conduit. In order to understand

89 better the timescales for sealing tuffisite veins at depth, we have carried out experiments in  
90 which ash-sized particles of natural obsidian are sintered in H<sub>2</sub>O fluid at high vapor pressures.

91

## 92 **Methods**

93 Rhyolitic obsidian that consists of clear rhyolitic glass and less than 1 vol.% microlites of Fe-Ti  
94 oxides was used in all experiments. Previous work has found that the glass has a dissolved H<sub>2</sub>O  
95 content of ~0.15 wt.% (J. Gardner, unpub. data). The obsidian was crushed into pieces with a  
96 steel mortar and pestle, and then those pieces were ground to a powder using an agate mortar and  
97 pestle. Some of the powder was sieved before being used in experiments, which we term  
98 “sieved”; the remaining portion of the powder was used in “un-sieved” experiments. Splits of  
99 each sample were analyzed for their particle-size distribution (Fig. 1). We compute the  
100 arithmetic weighted mean of the distribution of particle sizes. This is done by computing the  
101 weighted sum by  $\bar{R} = \sum R_j \xi_j$ , where  $R_j$  is the  $j$ th particle radius bin and  $\xi_j$  is the volume fraction  
102 of the total particles in that bin. The un-sieved powder has a mean radius ( $\bar{R}$ ) = 89  $\mu\text{m}$ , but  
103 contains particles from 1 to ~1600  $\mu\text{m}$  (median radius ( $\tilde{R}$ ) = 66  $\mu\text{m}$ ). Grain sizes of the sieved  
104 sample are more uniform, with 90% of the sample (by volume) in the 126 to 250  $\mu\text{m}$  size range;  
105 overall,  $\bar{R} = 185 \mu\text{m}$  ( $\tilde{R} = 160 \mu\text{m}$ ). Although there is overlap in sizes between the two samples,  
106 half of the un-sieved sample is finer than any of the sieved sample (Fig. 1).

107 Each experiment consisted of ~30 mg of either sieved or un-sieved powder placed inside a  
108 Au capsule (3 mm O.D.) that was welded shut on one end. The other end of the capsule was left  
109 open. The capsule was placed into a sample holder at the end of an Inconel rod, which was then  
110 inserted into a pressure vessel that was fitted with a rapid quench extension, as described in



111 Gardner (2007). The pressure vessel was connected to the pressure line, and pressure was  
112 applied using H<sub>2</sub>O (either 20 MPa or 40 MPa). Because the capsule was open at one end, the  
113 pressurized H<sub>2</sub>O was in contact with the powder, and the pressure in the interstitial open pore  
114 space between the particles was equal to that in the pressure vessel. Because pressure inside and  
115 outside the capsule is the same, the capsule exerted no stress on the particles within, and the only  
116 stress driving sintering resulted from interfacial tension between the molten particles and  
117 interstitial H<sub>2</sub>O.

118 An external magnet held the sample rod in place, such that the sample remained inside a  
119 water-cooled jacket while the pressure vessel was heated to the desired experimental  
120 temperature, as measured using K-type thermocouples precise to  $\pm 5^{\circ}\text{C}$ . Pressure was recorded  
121 with a pressure transducer that is precise to  $\pm 0.1$  MPa. Once the vessel equilibrated to the  
122 desired temperature, the external magnet was raised, lifting the sample into the hot zone of the  
123 pressure vessel in  $\sim 1$  second. Pressure dropped  $\sim 2.0$  MPa when the sample was raised, but was  
124 quickly readjusted to the desired value in  $\sim 15$  seconds. The sample was then held in place for 5  
125 to 90 minutes (Table 1). During that time, pressure varied by no more than 0.1 MPa and  
126 temperature varied by no more than  $1^{\circ}\text{C}$ . After the target time was reached, the magnet was  
127 lowered, bringing the sample into the water-cooled jacket where it cooled at  $\sim 150^{\circ}\text{C}$  per second  
128 (Dobson et al., 1989). When the sample was lowered, pressure increased by  $\sim 2.0$  MPa, but was  
129 quickly adjusted back to the experimental pressure in  $\sim 15$  seconds.

130 Samples were extracted from their Au capsules, and, if coherent, sealed in epoxy and thin  
131 sectioned to about 500  $\mu\text{m}$  thickness. A petrographic microscope was used to evaluate sample  
132 textures and measure vesicle numbers, shapes, and sizes. Vesicularity was measured by  
133 photographing samples in reflected light, and then using NIH *Image* to make binary images of

134 the photographs to measure vesicle areas relative to the entire area of the image. The area  
135 fraction of vesicles is converted directly to vesicle volume percent under the assumption that the  
136 vesicles are homogeneous throughout the sample and the pore network is isotropic, which is  
137 typical of sintering systems without a directional load applied (Wadsworth et al., 2016b). Errors  
138 on vesicularity are estimated at 10% of the measured value. The sizes of vesicles were measured  
139 using a graduated ocular on the petrographic microscope. Number density of vesicles ( $N_v$ ) was  
140 measured by selecting different areas in a sample and counting all vesicles that appear as the  
141 field of view is moved through it using the focusing knob of the microscope;  $N_v$  is thus number  
142 density per unit total volume (melt plus vesicles). The depth viewed was measured using a  
143 Heidenhain focus drive linear encoder. If more than one type of vesicle occurred in a sample  
144 (vesicle types are reported later), each vesicle type was counted and measured separately. All  
145 measured textures, vesicularities,  $N_v$  values, and mean vesicle sizes are reported in Table 1.

146 Area maps of OH, H<sub>2</sub>O<sub>m</sub>, and total H<sub>2</sub>O concentrations were made for four samples using a  
147 Thermo Nicolet Nexus 670 Fourier transform infrared (FTIR) spectrometer at the University of  
148 Oregon, following the methods of Watkins et al. (2017). All measurements were made using a  
149 15X objective, infrared source, MCT-A detector, and KBr beamsplitter, and absorbances were  
150 converted to concentrations using molar absorption coefficients for OH and H<sub>2</sub>O<sub>m</sub> from Zhang et  
151 al. (1997). The thickness of the sample was measured in several spots using a digital caliper with  
152 0.001 mm precision. Run settings for each map were as follows: 100 μm × 100 μm aperture,  
153 step size of 100 μm, spectral resolution of 4 cm<sup>-1</sup>, 64 scans per spot, and 64 scans for the  
154 background, which was collected every 10 minutes.

155 Experiments G1664 and G1647 were analyzed using attenuated total reflectance micro-  
156 Fourier transform infrared spectroscopy (ATR micro-FTIR). The analyses were performed using

157 a ThermoFisher Nicolet iN10 spectrometer and a Ge crystal at Bristol University (U.K). We  
158 measured evanescent wave absorption at 1630 and 3450  $\text{cm}^{-1}$ , which represent molecular ( $\text{H}_2\text{O}_m$ )  
159 and total water ( $\text{H}_2\text{O}_t = \text{H}_2\text{O}_m + \text{OH}$ ) species, respectively. An optical aperture of  $30 \times 30 \mu\text{m}$   
160 was used with an acquisition time of 25 seconds, resulting in 128 scans at a spectral resolution of  
161  $\sim 10 \text{ cm}^{-1}$ . Each analytical point was measured three times, and a new background spectrum was  
162 collected before every point. A linear background was applied from 1540-1700  $\text{cm}^{-1}$  for  $\text{H}_2\text{O}_m$   
163 and 2600-3700  $\text{cm}^{-1}$  for  $\text{H}_2\text{O}_t$ . Peak heights and the resulting  $\text{H}_2\text{O}$  species concentration were  
164 calculated following the methods and calibration of Lowenstern and Pitcher (2013).

165

## 166 **Results**

167

### 168 Experiments using Un-Sieved Powder

169

170 Overall, the vesicularities of samples coherent enough to section and measure decreased with  
171 time held at experimental temperature (Fig. 2a). The highest measured vesicularities are  $\sim 44$   
172 vol.%, but those samples are incipiently sintered. We can thus assume that the initial pore space  
173 of the particle pack was  $>44$  vol.%.

174 Five experiments were run at  $800^\circ\text{C}$  and 40 MPa for 5-60 minutes (Table 1). After 5 minutes,  
175 the sample was sufficiently sintered that it held together while it was extracted from the capsule  
176 and sectioned. Individual particles are, however, still clearly distinguishable (Fig. 3a). The  
177 particles are surrounded by an open, vesicular network that makes up  $\sim 30$  vol.% of the sample

178 (Fig. 3b). After 7 minutes, vesicularity had dropped to only 7 vol.%, but individual particle  
179 shapes are still discernable in some cases (Fig. 3c, d). Many vesicles are contorted, up to 500+  
180  $\mu\text{m}$  long, and retain the multi-cusped shapes that are a feature of the initial inter-particle pore  
181 space. Many other vesicles are spherical, and on average  $\sim 7 \mu\text{m}$  in diameter. Spherical vesicles  
182 are isolated from their neighbors. Contorted and spherical vesicles occur in roughly equal  
183 number densities (Table 1). By 10 minutes, the sample takes on the appearance of solid glass  
184 with vesicles dispersed in it, and the initially separate glass particles can only be discerned  
185 optically by differences in original microlite content; vesicularity dropped to 2.8 vol.% and the  
186 contorted vesicles are typically approximately 50-200  $\mu\text{m}$  long. Samples held longer than 10  
187 minutes also appear to be solid pieces of glass (Fig 3e, f), with similar vesicularities. Spherical  
188 vesicles occur throughout, but contorted vesicles decrease substantially in number, and are  
189 absent for run times  $>10$  minutes (Table 1). The average size of spherical vesicles increases with  
190 time, with the largest one observed being  $\sim 50 \mu\text{m}$  by 60 minutes.

191 Six experiments were run at  $750^\circ\text{C}$  and 40 MPa for 5-90 minutes (Table 1). The same  
192 progression in textural changes are found at these conditions as were found at  $800^\circ\text{C}$ , except that  
193 the changes took longer to evolve. Overall, vesicularity decreased from 44 vol.% at 5 minutes to  
194  $\sim 5$  vol.% at 90 minutes (Fig. 2a). Individual particles are discernable even after 15 minutes, and  
195 it is not until 20 minutes that samples appear to be solid glass with isolated vesicles dispersed in  
196 it. Isolated spherical vesicles formed by 15 minutes, but contorted vesicles persist for more than  
197 60 minutes. The number of contorted vesicles decreases with time, while spherical vesicles  
198 increase in both number and size (Table 1).

199 Four experiments were run at  $700^\circ\text{C}$  and 40 MPa for 5-60 minutes (Table 1). After 5  
200 minutes, the sample had not sintered enough to hold together, and so it crumbled when removed

201 from the capsule. After 15 minutes, sintering had progressed sufficiently to hold the sample  
202 together, but outlines of individual particles are easily seen and they are partially surrounded by a  
203 fully interconnected vesicle network that makes up ~18 vol.% of the sample (Fig. 2a). After 30  
204 minutes, outlines of individual particles are difficult to discern, but vesicles remain mainly  
205 interconnected, and make up about the same fraction of the sample as after 15 minutes. Only  
206 after 60 minutes did the sample appear to be solid glass with about 3 vol.% vesicles in it. Most  
207 vesicles, however, are still contorted in shape, and thin connections between neighboring  
208 vesicles are common.

209 Four experiments were run at 725°C and 20 MPa for 5-60 minutes (Table 1). Even after 15  
210 minutes, samples crumbled when removed from the capsule or during polishing. The sample  
211 that ran for 30 minutes was friable but partly held together when polished. It consists of  
212 individual particles that are only slightly sintered, separated by an open network of vesicles that  
213 make up ~38 vol.% of the sample (Fig. 2a). After 60 minutes, particles appear only slightly  
214 more sintered, making a slightly more cohesive sample, although vesicles are all interconnected  
215 and still occupy ~40 vol.% of the sample.

216

217 Experiments using Sieved Powder

218

219 All experiments with sieved powder were run at 40 MPa. As with the un-sieved powder, the  
220 vesicularities of samples decreased with time held at experimental temperature (Fig. 2b).  
221 Textures of the final products evolved similarly as in the un-sieved samples, but at different

222 rates. Compared to un-sieved samples run under the same conditions, at similar times, vesicles  
223 are fewer (lower  $N_v$ ) and larger (Fig. 4).

224 Two experiments were run at 800°C for 10 and 30 minutes (Table 1). After 10 minutes,  
225 particles have sintered with an interconnected network of vesicles between them. After 30  
226 minutes, all vesicles are isolated from their neighbors, but many are elongate in shape, rather  
227 than spherical (Fig. 4a).

228 Four experiments were run at 750°C for 30-90 minutes (Table 1). Vesicle textures evolve  
229 from an interconnected network at 30 minutes to isolated vesicles in dense glass at 60 minutes  
230 (Fig. 4c). After 45 minutes, vesicles are still contorted and occur in clusters in which they are  
231 locally connected to their neighbors by thin channels. Clusters are isolated, however, from  
232 neighboring clusters. Many vesicles are still contorted in shape, despite occupying only  $\leq 2$  vol.%  
233 of the sample (Fig. 4c).

234 Two experiments were run at 700°C for 60 and 90 minutes (Table 1). A fully open  
235 interconnected network of vesicles persisted after 90 minutes. Individual particles can still be  
236 discerned, although some of their contacts had melded together by 60 minutes.

237

238 H<sub>2</sub>O contents

239

240 H<sub>2</sub>O contents were mapped in four samples using transmission FTIR (G-1659, G-1643, G-1651,  
241 and G-1649). In all four, the distribution of H<sub>2</sub>O is relatively homogeneous, except where an  
242 analysis intersected large vesicles (Fig. 5). Compared with the majority of analyses, these

243 analyses tend to be anomalously low in H<sub>2</sub>O contents. We used the concentrations of H<sub>2</sub>O  
244 species to estimate cooling rate (Q), following Zhang et al. (1997), and found that Q correlates  
245 with H<sub>2</sub>O content (Fig. 5b, d). In general, the majority of analyses give Q >10 K s<sup>-1</sup>, in  
246 agreement with the known cooling rate of the experiment. Those that give Q <10 K s<sup>-1</sup> are those  
247 that are anomalously low in H<sub>2</sub>O contents and intersected vesicles. To determine H<sub>2</sub>O contents  
248 for each sample, therefore, we averaged only those analyses for which speciation indicates Q >10  
249 K s<sup>-1</sup>. Overall, we found average H<sub>2</sub>O contents of 2.4–2.6 wt.% (Table 1), in good agreement  
250 with H<sub>2</sub>O contents expected from solubility (Liu et al., 2005).

251 H<sub>2</sub>O contents of two samples (G–1664 and G–1647) were measured using ATR-FTIR. These  
252 analyses are restricted to the surface of the sample, and thus vesicles below the surface should  
253 not interfere. Overall, we found average H<sub>2</sub>O contents of 2.26±0.25 wt.% and 1.86±0.25 wt.%,  
254 respectively, for G–1664 and G–1647 (Table 1). The larger errors probably result from far fewer  
255 analyses per sample, compared to the FTIR maps (*n* = 11–17 versus 170–239). These values are  
256 relatively low, compared with H<sub>2</sub>O contents expected from solubility (Liu et al., 2005).

257

## 258 **Discussion**

259

260 The evolution of textures through the sintering process is similar in all sample suites. For  
261 convenience, we divide the evolution into four phases, but note that the progression between  
262 phases is continuous rather than discrete:

263 Phase 1) Particles are loose and cohesion-less.

264 Phase 2) Coherent but friable framework of still-discernable particles sintered at their  
265 contacts, interpenetrated by a continuous, tortuous pore space of up to ~40% (Fig. 3a, b).

266 Phase 3) Relict particle shapes still present, but vesicularity is  $\leq 10\%$  and no longer fully  
267 connected. Small isolated vesicles are spherical, but networks of larger vesicles remain  
268 multi-cusped in shape (Fig. 3c, d).

269 Phase 4) Dense glass with 2–5% fully isolated vesicles that are mainly spherical; a few larger  
270 vesicles can be more complex in shape (Fig. 3e, f; Fig. 4).

271 Our results show that sintering progresses more rapidly at higher temperature at a given pressure;  
272 un-sieved particles at 800°C reached Phase 4 in  $\leq 15$  minutes, but at 700°C did not reach Phase 4  
273 within the 60 minute duration of this experiment. In addition, sintering progressed more slowly  
274 at 725°C and 20 MPa than it did at 700°C and 40 MPa, suggesting that lowering the pressure  
275 (i.e., decreasing  $H_2O_t$ ) had a stronger influence than raising the temperature. Finally, sieved  
276 samples, with a larger mean particle size, progress through the phases more slowly under the  
277 same conditions (Fig. 2).

278 Equation 1 and the analysis that underpins it indicate that the sintering timescale,  $\lambda_s$ , is  
279 proportional to viscosity of the sintering particles (differences in surface tension are small for the  
280 ranges in dissolved  $H_2O$  content and temperature of our experiments and so we use an  
281 approximate value of surface tension of  $0.22 \text{ N m}^{-1}$  throughout; Bagdassarov et al., 2000;  
282 Gardner and Ketcham, 2011). Consequently, we infer that the variations in the rate of progress  
283 across the sintering phases resulted primarily from differences in melt viscosity. The two main  
284 variables that differ between experiments are temperature and pressure. Temperature directly  
285 controls viscosity through its effect on the mobility of network-forming cations Si and Al (Hess



286 and Dingwell, 1996). Additionally, temperature and pressure indirectly affect viscosity through  
287 their control on the H<sub>2</sub>O content of the melt (cf. Liu et al., 2005), which, in turn, directly impacts  
288 melt viscosity (Hess and Dingwell, 1996). Assuming that the particles have dissolved H<sub>2</sub>O  
289 contents equal to the equilibrium solubility (tested in the next subsection), we estimate that the  
290 viscosity (which we term  $\eta_e$  at equilibrium solubility) of samples held at 40 MPa and at 700°,  
291 750°, and 800°C would be  $\eta_e \approx 10^{7.1}$ ,  $10^{6.5}$ , and  $10^{6.0}$  Pa s, respectively (Hess & Dingwell,  
292 1996). Those held at 20 MPa and 725°C should be the most viscous, with  $\eta_e \approx 10^{7.5}$  Pa s.

293 The direct control of melt viscosity on the progression of sintering is apparent when changes  
294 in texture are considered as functions of time (Fig. 6). Samples with  $\eta_e \approx 10^{7.5}$  Pa s remain in  
295 Phase 1 conditions for ~30 minutes, but for less than 5 minutes at  $\eta_e < 10^{7.0}$  Pa s. Fully closed  
296 vesicularity (Phase 4) is reached in less than 10 minutes at  $\eta_e \approx 10^{6.0}$  Pa s, but takes ~25 minutes  
297 at  $\eta_e = 10^{6.5}$  Pa s, and is not reached by 60 minutes at  $\eta_e > 10^{6.5}$  Pa s. In addition, final stable  
298 vesicularities of ~2–5 vol.% are reached in 10 minutes at  $\eta_e \approx 10^{6.0}$  Pa s, 20 minutes at  $\eta_e \approx 10^{6.5}$   
299 Pa s, and 60 minutes at  $\eta_e \approx 10^{7.0}$  Pa s (Fig. 2).

300 The competition between the rates of hydration and sintering is expected to be important for  
301 sintering behavior. If hydration is long compared with sintering, we expect the particles to  
302 maintain their initial H<sub>2</sub>O content through the sintering process, and hence the controlling  
303 viscosity will be that given by the initial H<sub>2</sub>O content and temperature. Given that textures  
304 evolved more slowly at lower pressure despite a higher temperature, this seems unlikely. If,  
305 instead, hydration is fast compared with sintering, we expect the particles to reach their  
306 equilibrium solubility H<sub>2</sub>O contents early in the sintering process, and hence the controlling  
307 viscosity will be that given by the solubility H<sub>2</sub>O content. To explore this in more detail, we now

308 compare the expected timescale of ash hydration during the experiments with the timescale of  
309 sintering.

310

311 Timescale of hydration

312

313 The obsidian glass has an initial water content of 0.15 wt.%, which is lower than the equilibrium  
314 H<sub>2</sub>O solubility expected at the experimental conditions (Liu et al., 2005). This means that  
315 particles are undersaturated at the start of the experiments, and will hydrate as H<sub>2</sub>O progressively  
316 dissolves and diffuses into them. Hydration will advance from rim to core over time, resulting in  
317 a time-dependent spatial gradient of viscosity, with lower viscosity at the rim, and higher  
318 viscosity in the core. Furthermore, small particles are expected to hydrate more rapidly than large  
319 particles. We now test the assumption, made earlier, that particles are fully hydrated during the  
320 course of the experiments.

321 Hydration is diffusion-limited, such that there is a characteristic timescale over which the  
322 H<sub>2</sub>O content of the particles approaches equilibrium with the H<sub>2</sub>O solubility at experimental  
323 conditions. This hydration timescale  $\lambda_d$  is given by

324

$$\lambda_d = \frac{\bar{R}^2}{D} \quad (2)$$

325

326 where  $D$  is diffusivity of H<sub>2</sub>O in the silicate melt. We can estimate whether a particle is expected  
327 to be fully hydrated by comparing the hydration timescale with the time  $t$  for which the particle

328 is held at experimental conditions. The ratio of these timescales gives the dimensionless Fick  
329 number (Fi):

330

$$Fi = \frac{t}{\lambda_d} = \frac{Dt}{R^2}. \quad (3)$$

331

332 For  $Fi \gg 1$ , hydration is expected to be complete; for  $Fi \ll 1$  hydration is expected to be  
333 negligible; and for  $Fi$  on order of one particles are expected to be partially hydrated. We note,  
334 however, that a scaling analysis of this sort cannot be used *ab initio* to predict the value of  $Fi$  that  
335 divides the hydrated and unhydrated regimes – that requires empirical data.

336 In order to compute  $\lambda_d$ , and hence  $Fi$ , for a specific experiment, we must first calculate  
337 diffusivity, which depends on pressure, temperature, and dissolved water concentration. We use  
338 the empirical law for diffusivity of total water of Zhang and Ni (2010), which is calibrated for  
339 rhyolite over the range of conditions under consideration:

340

$$D = C \exp \left[ a_1 + a_2 P - \left( \frac{a_3 + a_4 P}{T} \right) \right] \quad (4)$$

341

342 where  $C$  is dissolved water content of the melt in wt.%,  $P$  and  $T$  are in MPa and K, respectively,  
343 and  $a_1 = -18.1$ ,  $a_2 = 1.888 \times 10^{-3}$ ,  $a_3 = 9699$ , and  $a_4 = 3.626$  are constants. Our experiments are  
344 run under isothermal and isobaric conditions, hence  $D$  depends only on  $C$  during the experiment.

345 The H<sub>2</sub>O concentration at equilibrium solubility,  $C_e$ , in the absence of other volatile species, is  
346 given by (Liu et al., 2005):

347

$$C_e = \frac{b_1 P^{0.5} + b_2 P - b_3 P^{1.5}}{T} + b_4 P^{1.5} \quad (5)$$

348

349 where  $b_1 = 354.941$ ,  $b_2 = 9.623$ ,  $b_3 = 1.5223$ , and  $b_4 = 0.0012439$  are empirical constants.

350 Figure 7 plots the measured dissolved water concentrations against those expected at  
351 equilibrium solubility, calculated from Eqn. 5, with diffusivity calculated at equilibrium  
352 solubility via Eqns. 4 and 5. The four samples for which  $Fi > 1$  lie very close to the 1:1 line,  
353 indicating that the assumption of full hydration is valid for those samples. The two samples for  
354 which  $Fi < 1$  have measured water concentrations slightly lower than the equilibrium value,  
355 indicating that these samples are not fully hydrated. The success of this analysis indicates that  
356 Fick number is an effective measure of the degree of hydration, and that the boundary between  
357 hydrated and unhydrated regimes is indeed near  $Fi = 1$  when using the water concentration at  
358 equilibrium solubility instead of the initial water concentration. Fick numbers have been  
359 calculated for all experiments, assuming equilibrium H<sub>2</sub>O concentrations (Table 1).  $Fi$  is close to  
360 or greater than 1 for most, implying that the particles in most of the samples can be considered  
361 completely hydrated on the timescales of the experiments.

362

363 Modelling sintering of ash particles at elevated vapor pressure

364

365 The ratio of sintering and diffusion timescales gives a dimensionless capillary Peclet number  
366 (Wadsworth et al., 2017)

367

$$Pc = \frac{\lambda_d}{\lambda_s} = \frac{\sigma \bar{R}}{\eta D}. \quad (6)$$

368

369 Note that this formulation includes the implicit assumption that the length scale in Eqn. 1 is  
370 taken as the particle radius. The capillary Peclet number is of use when we must consider  
371 whether time dependent changes in  $\eta$  or  $D$  will have a significant impact on the sintering  
372 process. When  $Pc \gg 1$ , diffusion is slow compared with sintering, in which case, the time  
373 dependent mass transfer of water and resultant changes in  $D$  and  $\eta$  can be neglected, and  
374 sintering will be governed by the initial water content  $C_i$  and the associated viscosity  $\eta_i$ . When  
375  $Pc \ll 1$ , diffusion is fast compared with sintering, in which case time dependent changes in  $\eta$  or  
376  $D$  can again be neglected, but sintering will be controlled by the solubility value of water  $C_e$  and  
377 the associated viscosity  $\eta_e$ . For intermediate values of  $Pc$ , time-dependent changes may be  
378 important, and should be accounted for in any modelling analysis. As was the case for the Fick  
379 number, this scaling analysis cannot be used *ab initio* to predict the value of  $Pc$  that divides the  
380 regimes.

381 We use Eqns. 4 and 5 to find  $D$  at equilibrium solubility, and the model of Hess and  
382 Dingwell (1996) to calculate the associated  $\eta_e$  for each set of experimental  $P$ ,  $T$  conditions, and  
383 then calculate  $Pc$  via Eqn. 6. We find capillary Peclet numbers in the intermediate range ( $0.25 <$   
384  $Pc < 9$ ), indicating that further investigation is required to determine into which regime our

385 experiments fall. We do this by comparing our experimental data with the sintering model of  
386 Wadsworth et al. (2014), who showed that the porosity of a sintering pack of angular glass  
387 particles evolves over time according to the equation

388

$$\phi = \phi_i \exp\left[-\frac{3t}{2\lambda_s}\right], \quad (7)$$

389

390 where  $\phi$  is volume fraction of vesicles, and  $\phi_i$  is the initial volume fraction of the sample before  
391 sintering begins, approximated as 60 vol.%, which is reasonable for random close packing of  
392 rough, angular particles (Mader et al., 2013; Wadsworth et al., 2014). This model has been  
393 shown to give a good approximation to a full sintering model (Wadsworth et al., 2016b), and is  
394 used for convenience because of its analytical tractability.

395 We model the evolution of porosity through sintering under two scenarios: 1)  $\lambda_s$  in Eqn. 7 is  
396 calculated (Eqn. 1) using  $\eta_i$ , which is equivalent to assuming that  $Pc \gg 1$ ; 2)  $\lambda_s$  is calculated  
397 using  $\eta_e$ , which is equivalent to assuming that  $Pc \ll 1$ . Curves are plotted for each scenario in  
398 figure 8, in which we normalize the experimental times by the appropriate  $\lambda_s$  to yield a  
399 dimensionless time. We find poor agreement between the predicted evolution of porosity (Eqn.  
400 7) and the experimental data scaled according to scenario (1) (Fig. 8a). In contrast, there is much  
401 better agreement with scenario (2) (Fig. 8b). This argues that the experiments fall in the low  
402 capillary Peclet number behavioral regime, despite having values of  $Pc$  near unity. This is  
403 important, because it demonstrates that our experiments faithfully model behavior at equilibrium  
404 conditions at elevated pressure and temperature.

405        Although our experiments dominantly capture behavior in the low capillary Peclet regime,  
406 there is some evidence of behavior that would be expected at intermediate capillary Peclet  
407 number. A manifestation of progressive hydration is that the rims of particles reach low  
408 viscosity and become mobile before the particle interiors. This means that particle contacts can  
409 weld together before wholesale sintering takes place, resulting in samples reaching Phase 2  
410 relatively quickly, but individual particle shapes remaining discernable for extended periods of  
411 time. Furthermore, small particles hydrate more rapidly than large particles, allowing them to  
412 fill in gaps between larger particles, leading to the formation of spherical vesicles relatively early  
413 in the sintering process (Phase 2), while larger, contorted vesicles take much longer to become  
414 spherical. The absence of small, hydrated particles in the sieved samples explains why they took  
415 longer to texturally evolve (Fig. 2), and why contorted vesicles remain longer (Fig. 4a, c).

416

417 Implications for tuffisite longevity

418

419 Our results provide a framework for understanding sintering of ash particles at high fluid  
420 pressures. Importantly, sintering was found to evolve at different rates, depending on pressure  
421 and temperature conditions and particle size. Such complexities are likely to be relevant in  
422 natural tuffisite veins, because volatile elements are thought to migrate through them after their  
423 formation (Berlo et al., 2013; von Aulock et al., 2013; Castro et al., 2014). Our analysis shows  
424 that we can predict sintering dynamics in scenarios where hydration precedes thorough sintering  
425 by using the viscosity at equilibrium water solubility in the low capillary Peclet number regime,  
426 and when particles are not monodisperse (given by  $\bar{R}$ ) – conditions relevant to tuffisite closure.

427 Our model predicts that the vesicularity of tuffisite veins will decrease substantially as ash  
428 within them sinters to glass. Figure 8 shows that the vesicularity of the sintering ash drops over a  
429 fairly short dimensionless time window: rapid decrease in vesicularity begins only once  $t \gtrsim$   
430  $0.5\lambda_s$ , and the final, fully-dense value is reached by  $t \approx 2\lambda_s$ . Consequently,  $t = \lambda_s$  is a useful  
431 approximate measure for the timescale of densification and, therefore, of the timescale over  
432 which tuffisite veins are expected to seal and become impermeable. In terms of dimensional  
433 variables, the sealing time depends on temperature and pressure (via their control on viscosity)  
434 and on the size of the ash particles (Eqn. 1). To illustrate the variation in sealing time, we  
435 calculate  $\lambda_s$  as a function of depth in a magma-filled conduit (Fig. 9). The equilibrium solubility  
436  $C_e$  was calculated as a function of depth, via equation 5, for  $T = 700, 800, \text{ and } 900^\circ\text{C}$ ; pressure  
437 was calculated assuming hydrostatic conditions and a constant density of  $2000 \text{ kg m}^{-3}$ . From this,  
438  $\eta_e$  was calculated as a function of depth after Hess and Dingwell (1996). Particle sizes were  
439 fixed at either  $10 \text{ }\mu\text{m}$  (Fig. 9a) or  $100 \text{ }\mu\text{m}$  (Fig. 9b), and  $\lambda_s$  was calculated from equation 1.  
440 Using these simplifying assumptions, we find that for rhyolite at  $800^\circ\text{C}$ , the timescale for  
441 sintering of fine ash ( $10 \text{ }\mu\text{m}$ ) to dense glass is less than a few minutes throughout most of the  
442 conduit. In contrast, cold, coarse rhyolitic ash at depths less than  $\sim 2 \text{ km}$  takes hours to sinter  
443 (Fig. 9).

444 Figure 9 also plots the diffusion timescale  $\lambda_d$  for the same conditions, assuming diffusivity at  
445 equilibrium solubility. For a given depth, temperature, and particle size, if  $\lambda_d < \lambda_s$ , then  $\text{Pc} < 1$ .  
446 Our experiments were run in the low Peclet number regime, hence our results are valid for  $\text{Pc} <$   
447  $1$ . Furthermore, our experiments were run using natural materials at conduit conditions, so our  
448 results can be applied directly to the natural case, with no further scaling, in this regime. Our



449 results show that for a given temperature smaller particles spend more time in the shallow  
450 conduit in the low  $Pc$  regime.

451 In figure 10, we present a regime plot that shows the position of the  $Pc = 1$  curve in  
452 temperature–depth space, for particles of different radius. This plot can be used to determine the  
453 approximate conditions under which the analysis presented in this work can be applied to the  
454 natural case. For each line, the low Peclet number regime is towards lower temperature and  
455 shallower depth. For example, for magma at  $800^{\circ}\text{C}$  and 3000 m depth, a particle of  $10\ \mu\text{m}$  radius  
456 will sinter such that  $Pc = 1$ , so our analysis can be applied. We can also see that any smaller  
457 particle will sinter in the  $Pc < 1$  regime, as will a particle of  $10\ \mu\text{m}$  at lower temperature or  
458 shallower depth; our analysis therefore applies in all of these cases. By contrast, sintering of  
459 particles of 1 mm radius at  $750^{\circ}\text{C}$  and 1000 m depth will be in the  $Pc > 1$  regime. Consequently,  
460 diffusion will occur slowly compared with sintering, and our analysis is not valid. Note the  
461 additional condition that our analysis is only valid for particles that are either hydrating, or have  
462 water content that is approximately in equilibrium with the pressure and temperature conditions.

463 A substantial decrease in vesicularity does not necessarily cause a decrease in the flow of gas  
464 through a tuffisite vein, because permeability may still be high, depending on the tortuosity of  
465 the connected pore space (e.g., Saar and Manga, 1999). While we do not explicitly measure the  
466 permeability of the sintered samples, Wadsworth et al., (2016) and Wright and Cashman (2014)  
467 showed that the permeability of a welding pack of particles or a welding ignimbrite will decrease  
468 as porosity decreases. We observe that, when particles are only slightly to partially sintered  
469 (Phases 1–3), channels in the vesicular network can be traced visually through the sample, and  
470 hence the sample remains permeable. With time, those long-range channels seal off, and  
471 relaxation of the contorted vesicles creates spherical vesicles. Spherical to nearly spherical

472 vesicles are isolated, such that gas could not flow between them, hence samples that contain only  
473 spherical bubbles (i.e. at Phase 4) can be considered impermeable. At  $\eta_e = 10^6$  Pa s, we thus  
474 infer that sintering created impermeable samples in about 10 minutes (Fig. 6). In contrast, at  $\eta_e$   
475  $= 10^{7.5}$  Pa s, samples potentially remain permeable for more than 60 minutes. At relatively low  
476 viscosities, therefore, our results suggest that gas can flow through veins for only about 10–20  
477 minutes. If low viscosity magma containing veins thus ascended at a rate of  $0.5 \text{ m s}^{-1}$  (a  
478 reasonable assumption for the ascent of Chaiten magma while it simultaneously erupted and  
479 effused; Castro and Dingwell, 2009), it would rise only ~300–600 meters before the veins sealed.  
480 In contrast, the same magma with a viscosity of  $\geq 10^7$  Pa s would remain permeable for >60  
481 minutes, allowing it to degas while rising >1800 meters. Given that, as magma rises, solubility  
482 drops, viscosity increases, and sintering timescale becomes longer, fractures that develop in the  
483 upper few kilometers of the conduit may be able to rise all the way to the surface before they  
484 seal.

485 Natural tuffisites can contain textural complexity not captured by our model system. Namely,  
486 clasts in partially welded tuffisites are often internally vesiculated (e.g., Castro et al., 2012;  
487 Saubin et al., 2016), exhibit evidence of internal densification of a previously vesicular clast  
488 (e.g., Castro et al., 2014; Saubin et al., 2016), or exhibit evidence of shear strain (e.g., Tuffen and  
489 Dingwell, 2005). Tuffisites may also form in vesicular (Castro et al., 2012) or crystalline  
490 (Kendrick et al., 2016) magma, and are not necessarily hosted in dense obsidian. In these cases,  
491 the densification timescales may be modified by syn-sintering bubble nucleation and bubble  
492 growth in large clasts, shear deformation of the welding tuffisite, and the presence of crystals in  
493 the groundmass. Our model therefore represents the scenario in which the host and clast-fill are  
494 both dominantly glassy.

495

## 496 Conclusions

497

498 The textural evolution of ash particles sintering under the action of surface tension follows the  
499 same trend for all temperature and pressure conditions, and for different ash size distributions.  
500 The rate of sintering is given by the sintering timescale  $\lambda_s$  (Eqn. 1), which depends on the  
501 viscosity and size of the sintering particles. The porosity of a sintering pack of ash particles  
502 begins to drop appreciably around  $0.5\lambda_s$  after the onset of sintering and reaches its final value at  
503 around  $2\lambda_s$ , at which point the pack becomes impermeable. The timescale over which an ash-  
504 filled crack is able to transport gas can therefore be computed if pressure, temperature, and  
505 particle size are known or can be estimated.

506 Our experiments were run under hydrating conditions, largely in the low Peclet number  
507 regime (Eqn. 6), in which diffusion time is short compared with sintering time. Consequently,  
508 the sintering timescale is set by the viscosity under equilibrium H<sub>2</sub>O solubility, and our results  
509 are relevant to sintering under conditions of equilibrium or near-equilibrium H<sub>2</sub>O content. Our  
510 analysis can therefore be applied under low Peclet number conditions, which are favored by  
511 smaller particles, at shallower depth, and at lower temperatures. For reasonable estimates of  
512 natural magmatic conduits, low Peclet number conditions are met in the upper few kilometers.  
513 We nonetheless expect that conditions in natural tuffisite veins may sometimes lead to sintering  
514 under high Peclet number and/or dehydrating conditions. Our analysis cannot be applied under  
515 such conditions, and further experimental work is required to characterize sintering behavior in  
516 those regimes.

517

518 **Acknowledgements**

519 JEG was partially supported by a grant from the National Science Foundation (EAR-1348050). EWL  
520 and JPC acknowledge support from the UK Natural Environment Research Council via grant  
521 NE/N002954/1. Jérémie Vasseur is warmly thanked for discussion throughout.

522

523

524 **References**

- 525 Bagdassarov N, Dorfman A, Dingwell DB (2000) Effect of alkalis, phosphorus, and water on the  
526 surface tension of haplogranite melt. *Am Mineral* 85:33-40
- 527 Berlo K, Tuffen H, Smith VC, Castro JM, Pyle DM, Mather TA, Geraki K (2013) Element  
528 variations in rhyolitic magma resulting from gas transport. *Geochim Cosmochim Acta*  
529 121:436–451
- 530 Blank JG, Stolper EM, Carroll MR (1993) Solubilities of carbon dioxide and water in rhyolitic  
531 melt at 850 °C and 750 bars. *Earth Planet Sci Lett* 119:27–36
- 532 Cabrera A, Weinberg RF, Wrigh, HMN, Zlotnik S, Cas RAF. (2011) Melt fracturing and  
533 healing: A mechanism for degassing and origin of silicic obsidian. *Geology* 39:67-70
- 534 Castro JM, Dingwell DB (2009) Rapid ascent of rhyolite magma at Chaitén volcano. *Nature*  
535 461:780–783
- 536 Castro JM, Cordonnier B, Tuffen H, Tobin MJ, Puskar L, Martin MC, Bechtel HA (2012) The  
537 role of melt-fracture degassing in defusing explosive rhyolite eruptions at Volcán Chaitén.  
538 *Earth Planet Sci Lett* 333–334:63–69
- 539 Castro JM, Bindeman IN, Tuffen H, Schipper CI. (2014) Explosive origin of silicic lava:  
540 Textural and  $\delta D-H_2O$  evidence for pyroclastic degassing during rhyolite effusion. *Earth*  
541 *Planet Sci Lett* 405:52–61
- 542 Dobson PF, Epstein S, Stolper EM (1989) Hydrogen isotope fractionation between coexisting  
543 vapor and silicate glasses and melts at low pressure. *Geochim Cosmochim Acta* 53:2723–  
544 2730.
- 545 Eichelberger JC, Carrigan CR, Westrich HR, Price RH (1986) Non-explosive silicic volcanism.

546 Nature 323:598–602

547 Gardner JE (2007) Heterogeneous Bubble Nucleation in Highly Viscous Silicate Melts During  
548 Instantaneous Decompression from High Pressure. *Chem Geol.* 236:1-12

549 Gardner JE, Ketcham RA (2011) Bubble nucleation in rhyolite and dacite melts: Temperature  
550 dependence of surface tension. *Contrib Mineral Petrol* 162:929-943

551 Gonnermann H, Manga M (2003) Explosive volcanism may not be an inevitable consequence of  
552 magma fragmentation. *Nature* 426:432–435

553 Hess K–U, Dingwell DB (1996) Viscosities of hydrous leucogranitic melts: A non–Arrhenian  
554 model. *Am Mineral* 81:1297–1300

555 Jaupart C, Allegre CJ (1991) Gas content, eruption rate and instabilities of eruption regime in  
556 silicic volcanoes. *Earth Planet Sci Lett* 102:413–429

557 Kendrick JE, Lavallée Y, Varley NR, Wadsworth FB, Lamb OD, Vasseur J (2016) Blowing off  
558 steam: Tuffisite formation as a regulator for lava dome eruptions. *Front Earth Sci* 4:41

559 Liu Y, Zhang Y, Behrens H (2005) Solubility of H<sub>2</sub>O in rhyolitic melts at low pressure and a  
560 new empirical model for mixed H<sub>2</sub>O–CO<sub>2</sub> solubility in rhyolitic melts. *J Volcanol Geotherm*  
561 *Res* 143:219-235

562 Lowenstern JB, Pitcher BW (2013) Analysis of H<sub>2</sub>O in silicate glass using attenuated total  
563 reflectance (ATR) micro-FTIR spectroscopy. *Am Mineral* 98:1660–1668

564 Mader HM, Llewellyn EW, Mueller SP (2013) The rheology of two-phase magmas: A review  
565 and analysis. *J Volcanol Geotherm Res* 257:135–158

566 Michaut C, Bercovici D, Sparks RSJ (2009) Ascent and compaction of gas rich magma and the  
567 effects of hysteretic permeability. *Earth Planet Sci Lett* 282:258–267

568 Quane SL, Russell JK, Friedlander EA (2009) Time scales of compaction in volcanic systems.  
569 *Geology* 37:471–474

570 Saar MO, Manga M (1999) Permeability–porosity relationship in vesicular basalts. *Geophys Res*  
571 *Lett* 26:111–114

572 Saubin E, Tuffen H, Gurioli L, Owen J, Castro JM, Berlo K, McGowan EM, Schipper CI,  
573 Wehbe K (2016) Conduit dynamics in transitional rhyolitic activity recorded by tuffisite  
574 vein textures from the 2008–2009 Chaitén eruption. *Front Earth Sci* 4:59

575 Schipper CI, Castro JM, Tuffen H, James MR, How P (2013) Shallow vent architecture during  
576 hybrid explosive–effusive activity at Cordón Caulle (Chile, 2011–12): evidence from direct  
577 observations and pyroclast textures. *J Volcanol Geotherm Res* 262:25–37

578 Stasiuk MV, Barclay J, Carroll MR, Jaupart C, Ratté JC, Sparks RSJ, Tait SR (1996) Degassing  
579 during magma ascent in the Mule Creek vent (USA). *Bull Volcanol* 58:117–130

580 Tuffen H, Dingwell DB (2005) Fault textures in volcanic conduits: evidence for seismic trigger  
581 mechanisms during silicic eruptions. *Bull Volcanol* 67:370–387

582 Tuffen H, Dingwell DB, Pinkerton H (2003) Repeated fracture and healing of silicic magma  
583 generate flow banding and earthquakes? *Geology* 31:1089–1092

584 Vasseur J, Wadsworth FB, Lavallée Y, Hess K-U, Dingwell DB (2013) Volcanic sintering:  
585 timescales of viscous densification and strength recovery. *Geophys Res Lett* 40:1–7

586 Von Aulock FW, Nichols ARL, Kennedy BM, Oze C (2013) Timescales of texture development  
587 in a cooling lava dome. *Geochim Cosmochim Acta* 114:72–80.

588 Wadsworth FB, Vasseur J, Aulock FW, Hess KU, Scheu B, Lavallée Y et al. (2014)  
589 Nonisothermal viscous sintering of volcanic ash. *J Geophys Res Solid Earth* 119:8792–8804

590 Wadsworth FB, Vasseur J, Scheu B, Kendrick JE, Lavallée Y, Dingwell DB (2016a) Universal  
591 scaling of fluid permeability during volcanic welding and sediment diagenesis. *Geology*  
592 44:219–222.

593 Wadsworth FB, Vasseur J, Llewellyn EW, Schaubert J, Dobson KJ, Scheu B, Dingwell DB  
594 (2016b) Sintering of viscous droplets under surface tension. *Proc Roy Soc A* 472:20150780.

595 Wadsworth FB, Vasseur J, Llewellyn EW, Genareau K, Cimarelli C, Dingwell DB (2017) Size  
596 limits for rounding of volcanic ash particles heated by lightning. *J Geophys Res Solid Earth*  
597 122:1977–1989

598 Watkins JM, Gardner JE, Befus KS (2017) Nonequilibrium degassing, regassing, and vapor  
599 fluxing in magmatic feeder systems. *Geology* 45:183–186

600 Wright HM, Cashman KV (2014) Compaction and gas loss in welded pyroclastic deposits as  
601 revealed by porosity, permeability, and electrical conductivity measurements of the Shevlin  
602 Park Tuff. *Geol Soc Am Bull* 126:234–247

603 Zhang Y, Ni H (2010) Diffusion of H, C, and O components in silicate melts. *Rev Mineral*  
604 *Geochem* 72:171–225.

605 Zhang Y, Belcher R, Ihinger PD, Wang L, Xu Z, Newman S (1997) New calibration of infrared  
606 measurement of dissolved water in rhyolitic glasses. *Geochim Cosmochim Acta* 61:3089-  
607 3100.



608 **Figure Captions**

609

610 **Figure 1:** Particle size distributions of powders used in experiments: **a)** “un-sieved” powder with  
611 sizes from 1 to 1000  $\mu\text{m}$ ; **b)** “sieved” powder with a narrower range of sizes; the approximate  
612 positions of the median ( $\tilde{R}$ ) and mean ( $\bar{R}$ ) particle sizes are shown for each.

613

614 **Figure 2:** Vesicularity (vol.%) of sintered samples of **a)** un-sieved and **b)** sieved obsidian  
615 powder as a function of time (errors on vesicularity are roughly 10% of the measured value):  
616 open squares for 800°C and 40 MPa; inverted triangles for 750°C and 40 MPa; diamonds for  
617 700°C and 40 MPa; and triangles for 725°C and 20 MPa; sieved samples are in gray. Lines are to  
618 guide the eye only.

619

620 **Figure 3:** Photomicrographs showing textures of sintered ash at 800°C (scale bar in each is 200  
621  $\mu\text{m}$  long). **a)** and **b)** Individual particles can still be clearly distinguished amongst tortuous  
622 vesicular network after 5 minutes (reflected and transmitted light images of G–1642). **c)** and **d)**  
623 individual particles are still discernable, but porosity has decreased significantly after 7 minutes  
624 (reflected and transmitted light images of G–1659). **e)** and **f)** Dense glass with low vesicularity of  
625 only spherical vesicles after 60 minutes (reflected and transmitted light images of G–1641).

626

627 **Figure 4:** Photomicrographs showing the differences in textures resulting from sintering of  
628 sieved ash [**a**) and **c**)] versus un-sieved ash [**b**) and **d**)] at 40 MPa (scale bar in each is 200  $\mu\text{m}$   
629 long). **a**) and **b**) were run at 800°C for 30 minutes. **c**) and **d**) were run at 750°C for 60 minutes.

630

631 **Figure 5:** Apparent dissolved H<sub>2</sub>O concentrations and quench rates (Q in K s<sup>-1</sup>) for two samples:  
632 **a**) and **b**) G-1643; **c**) and **d**) G-1651. H<sub>2</sub>O was measured by transmission FTIR; Q is calculated  
633 from the speciation of dissolved H<sub>2</sub>O (see text). Low apparent H<sub>2</sub>O contents and slow Q (<10 K  
634 s<sup>-1</sup>) are artifacts due to analyses intersecting large vesicles.

635

636 **Figure 6:** Variations in sintering texture of un-sieved samples as a function of equilibrium melt  
637 viscosity,  $\eta_e$  (calculated at equilibrium H<sub>2</sub>O solubility  $C_e$  following Liu et al., 2005 and Hess &  
638 Dingwell, 1996) and experimental time; symbols are the same as those in Figure 2. Dashed lines  
639 are drawn to demark approximate fields of constant texture. In Phase 1, individual particles  
640 remain loose and lack cohesion. In Phase 2, particles are sintered only at their contacts and  
641 porosity is fully open; the sample at 30 minutes and  $\eta_e = 10^{7.5}$  Pa s only partly held together, and  
642 was thus at the boundary between Phases 1 and 2. In Phase 3, particles are nearly merged  
643 together and the vesicle texture is nearly sealed, but many vesicles are still multi-cusped shaped.  
644 In Phase 4, samples consist of dense glass with isolated vesicles.

645

646 **Figure 7:** Observed ( $\pm 1\sigma$  errors) versus expected H<sub>2</sub>O concentrations for samples, all at 40 MPa;  
647 symbols are those used in Figure 2. Solid line is 1:1 line. Samples in green are those for which

648 Fick number  $Fi > 1$  (Eqn. 3), indicating complete hydration by the end of the experiment.

649 Samples in yellow are samples for which  $Fi < 1$ , indicating incomplete hydration.

650

651 **Figure 8:** Model results for sintering of particles, shown as variations in vesicularity, assuming

652 **a)** initial (dry)  $H_2O$  contents yielding viscosities  $\eta_i$ , and **b)** equilibrium  $H_2O$  solubility contents

653 yielding viscosities  $\eta_e$ ; symbols are the same as Figure 2. Curves are calculated from equation 7.

654

655 **Figure 9:** Sintering timescales for **a)** 10  $\mu m$  and **b)** 100  $\mu m$  particles as functions of depth in a

656 conduit filled with rhyolite at 700° (green curve), 800° (brown curve), or 900°C (red curve).

657 Also shown are the diffusion timescales for the same temperatures (dashed curves). Conditions

658 for  $Pc < 1$  are met when the diffusion curve is to the left of the sintering curve.

659

660 **Figure 10:** Regime plot showing the position of the  $Pc=1$  curve in temperature–depth space for

661 particles of different radius. The framework that we present for estimating sintering time is valid

662 for sintering in the low Peclet number regime; this figure can be used to identify conditions that

663 satisfy that requirement. For any curve, particles of the corresponding size will sinter in the low

664 Peclet number regime if the temperature and depth plot to the left of the curve. Equivalently, for

665 any given temperature and depth, particle sizes for which the corresponding curve passes to the

666 right will sinter in the low Peclet number regime. For example, at 800°C and 3000 m depth,

667 particles of 10  $\mu m$  radius or smaller will sinter in the  $Pc < 1$  regime.

668

# Percentage of sample by volume

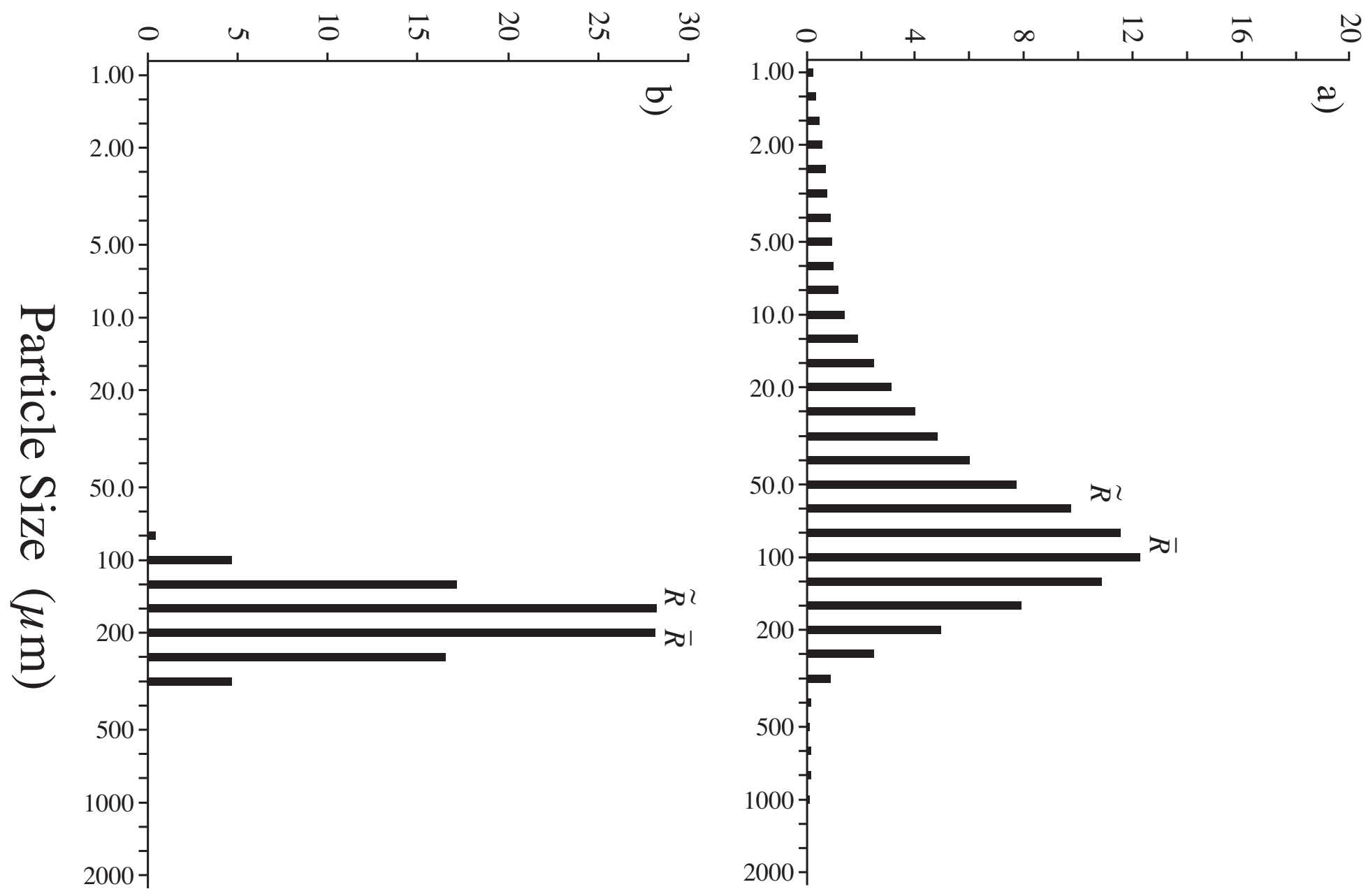


Figure 1

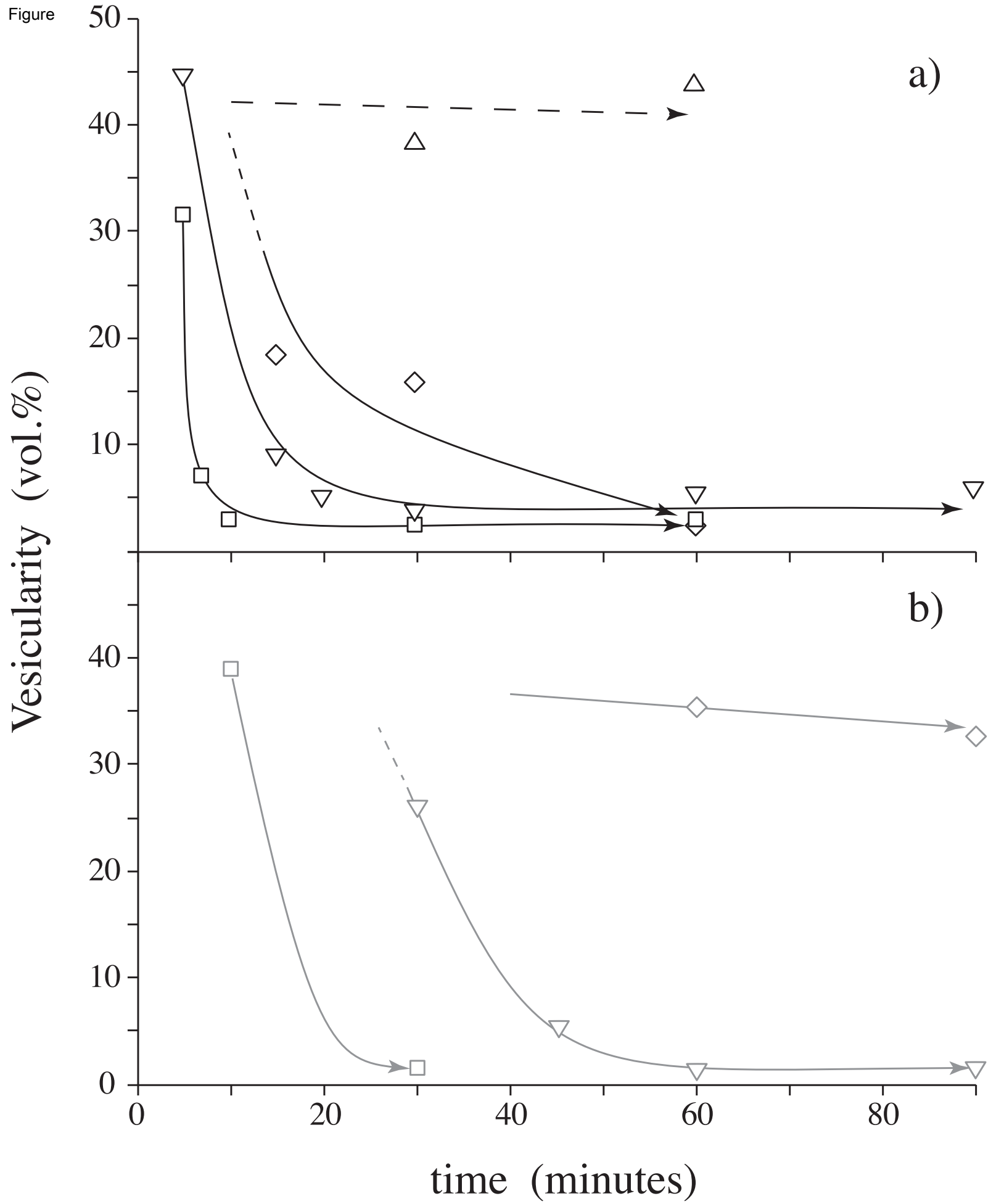


Figure 2

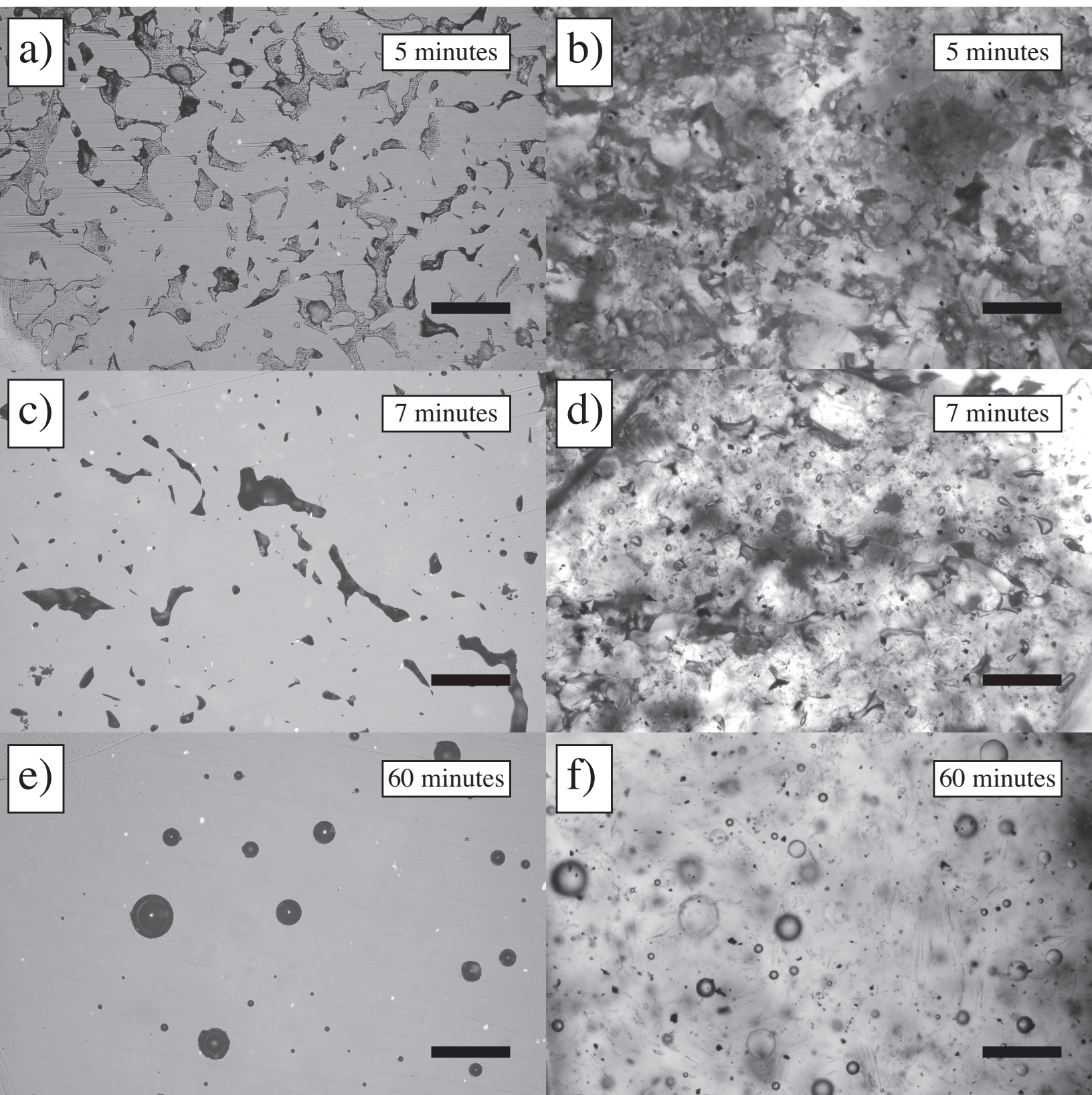


Figure 3

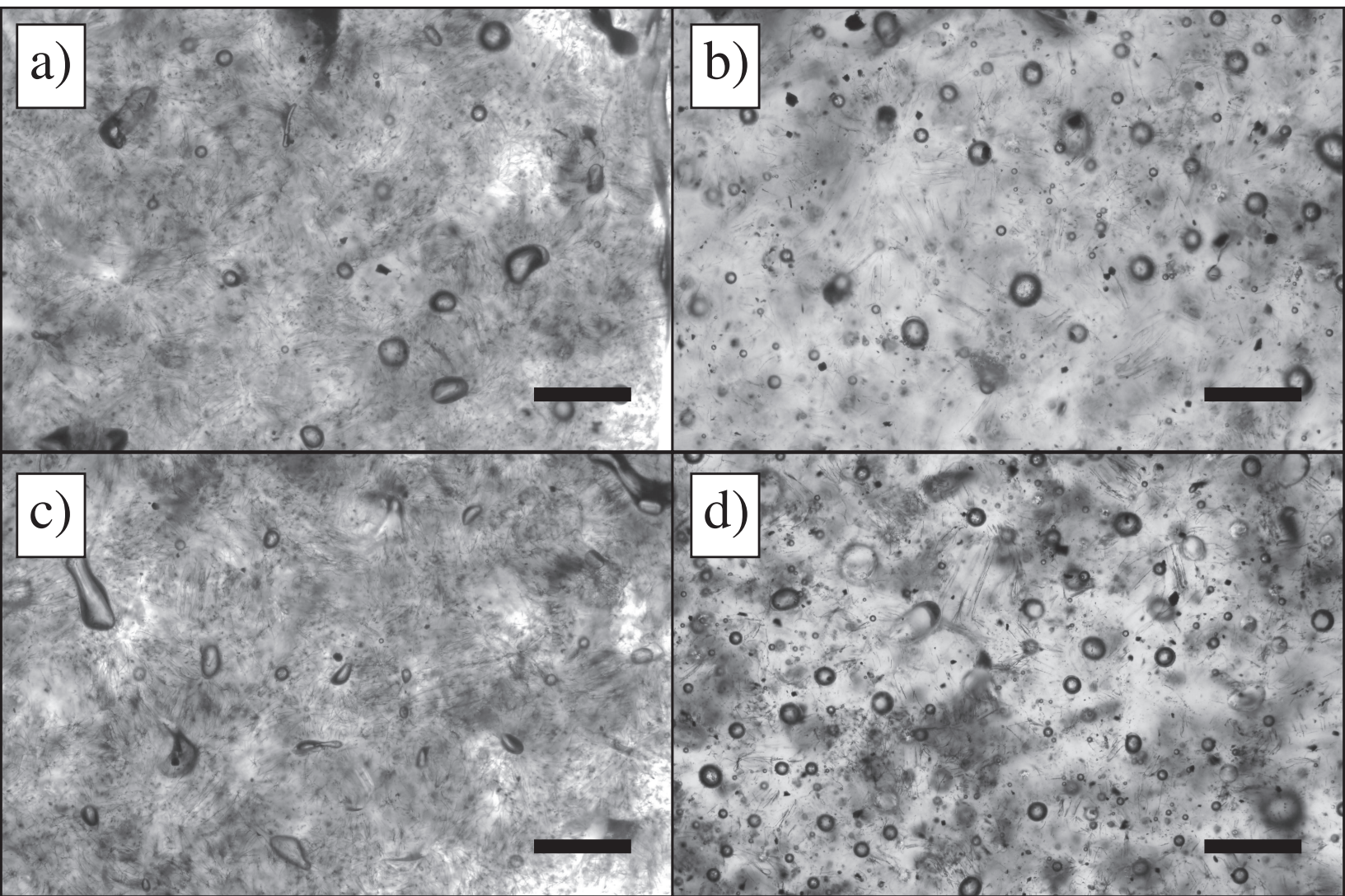


Figure 4

Figure

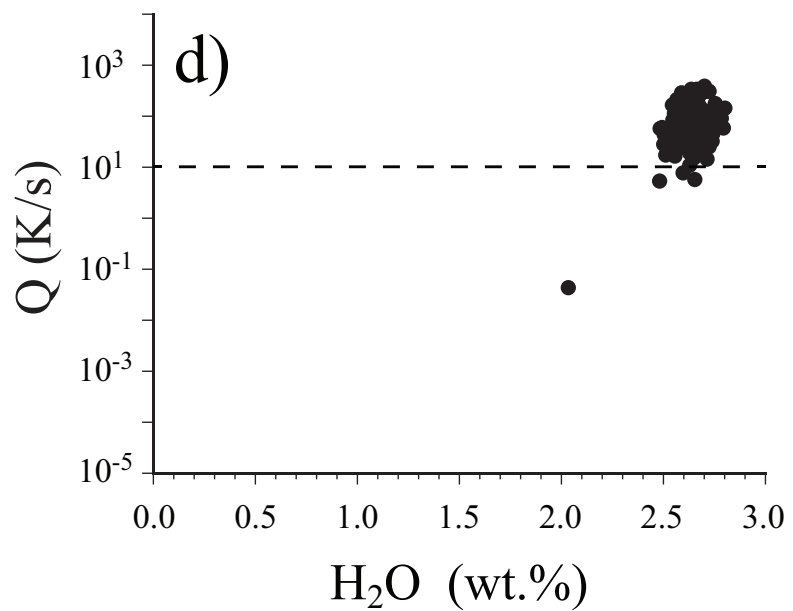
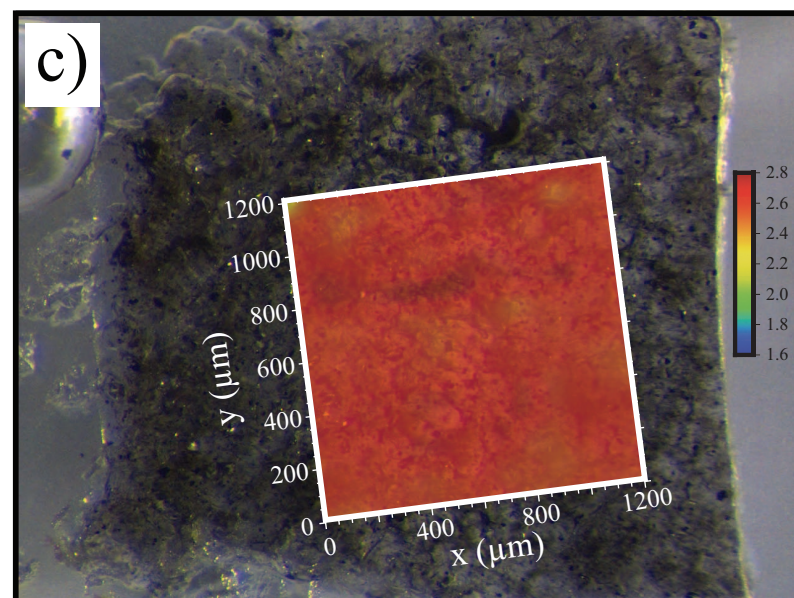
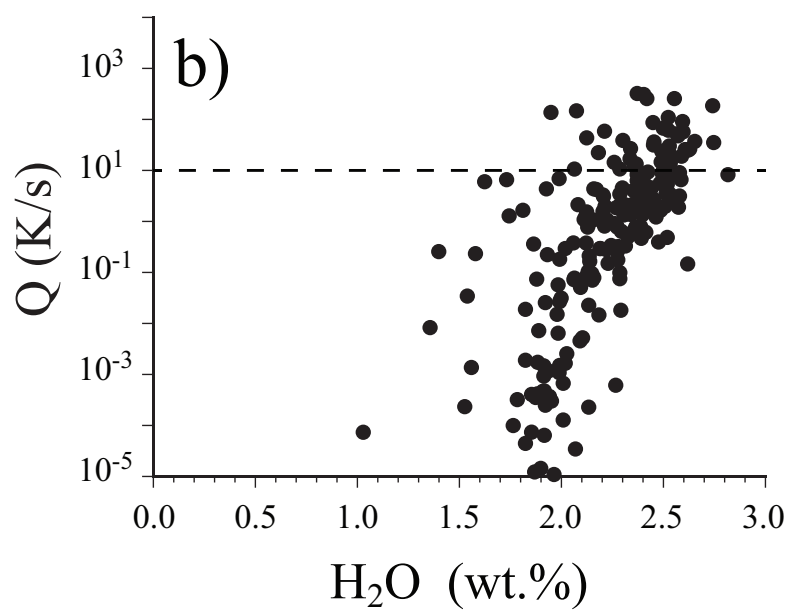
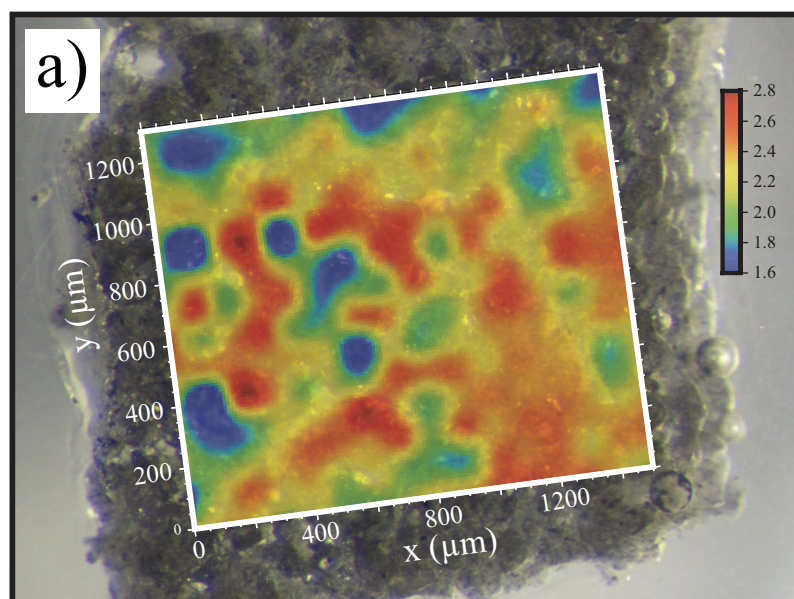


Figure 5



Figure

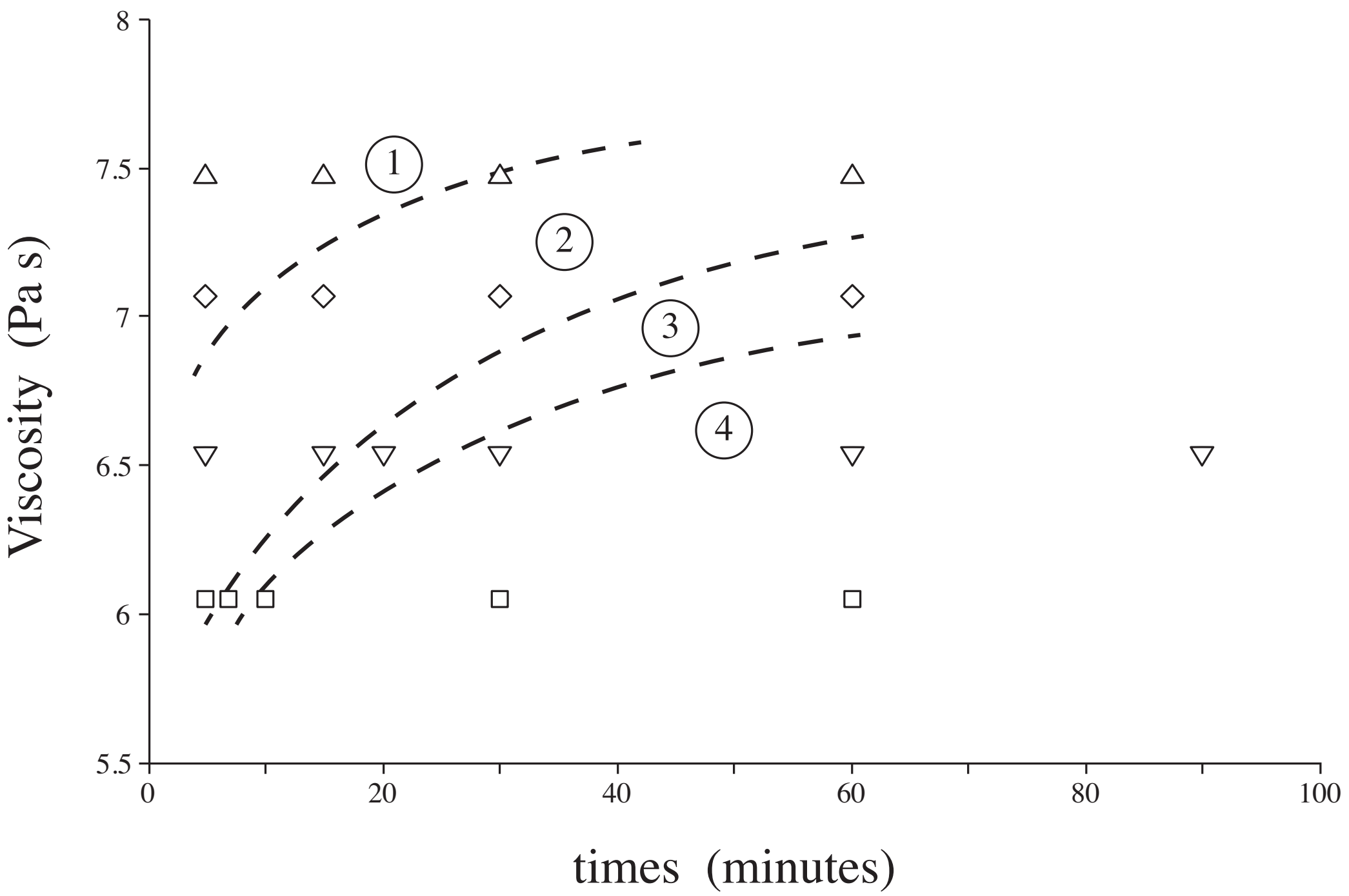


Figure 6

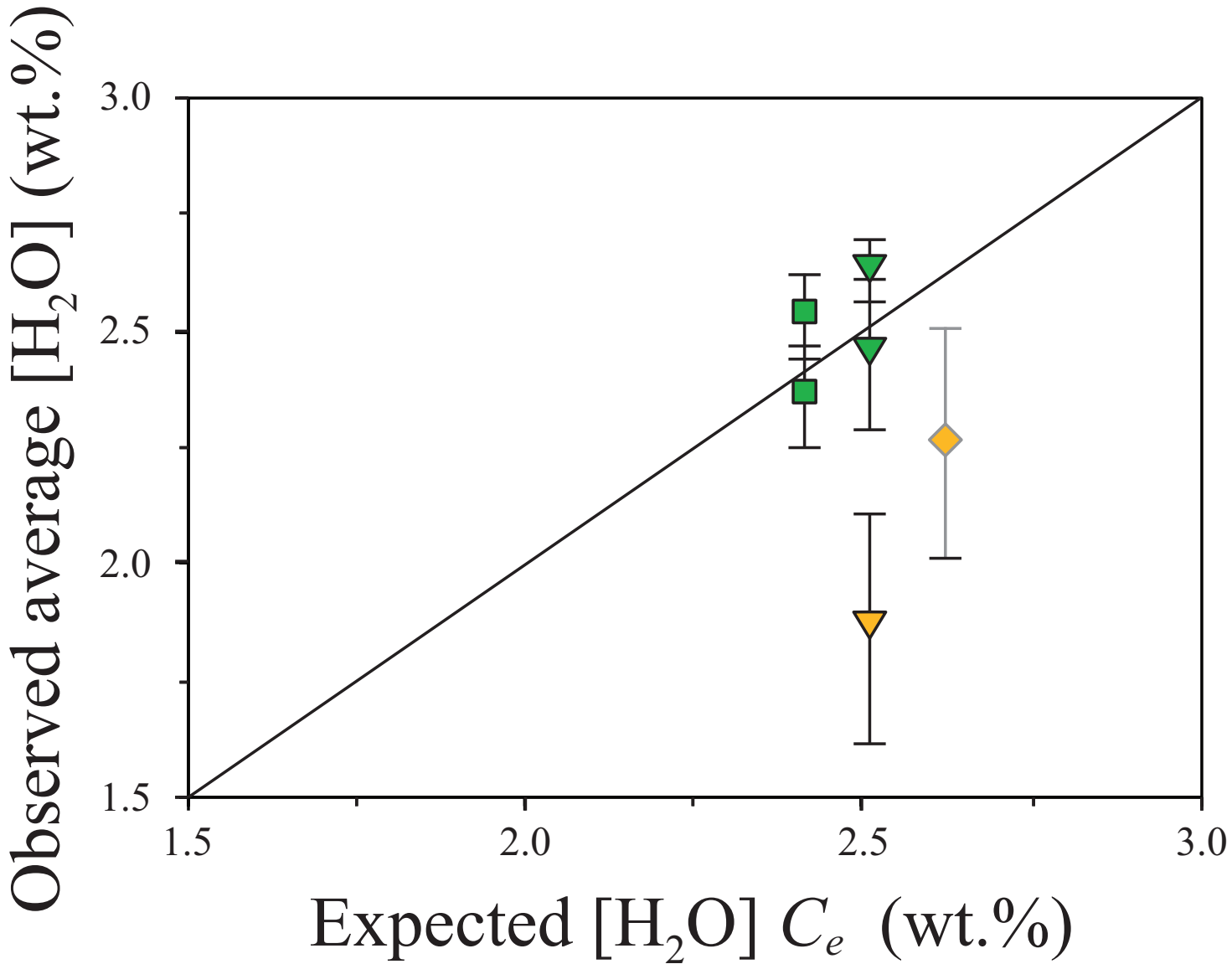


Figure 7

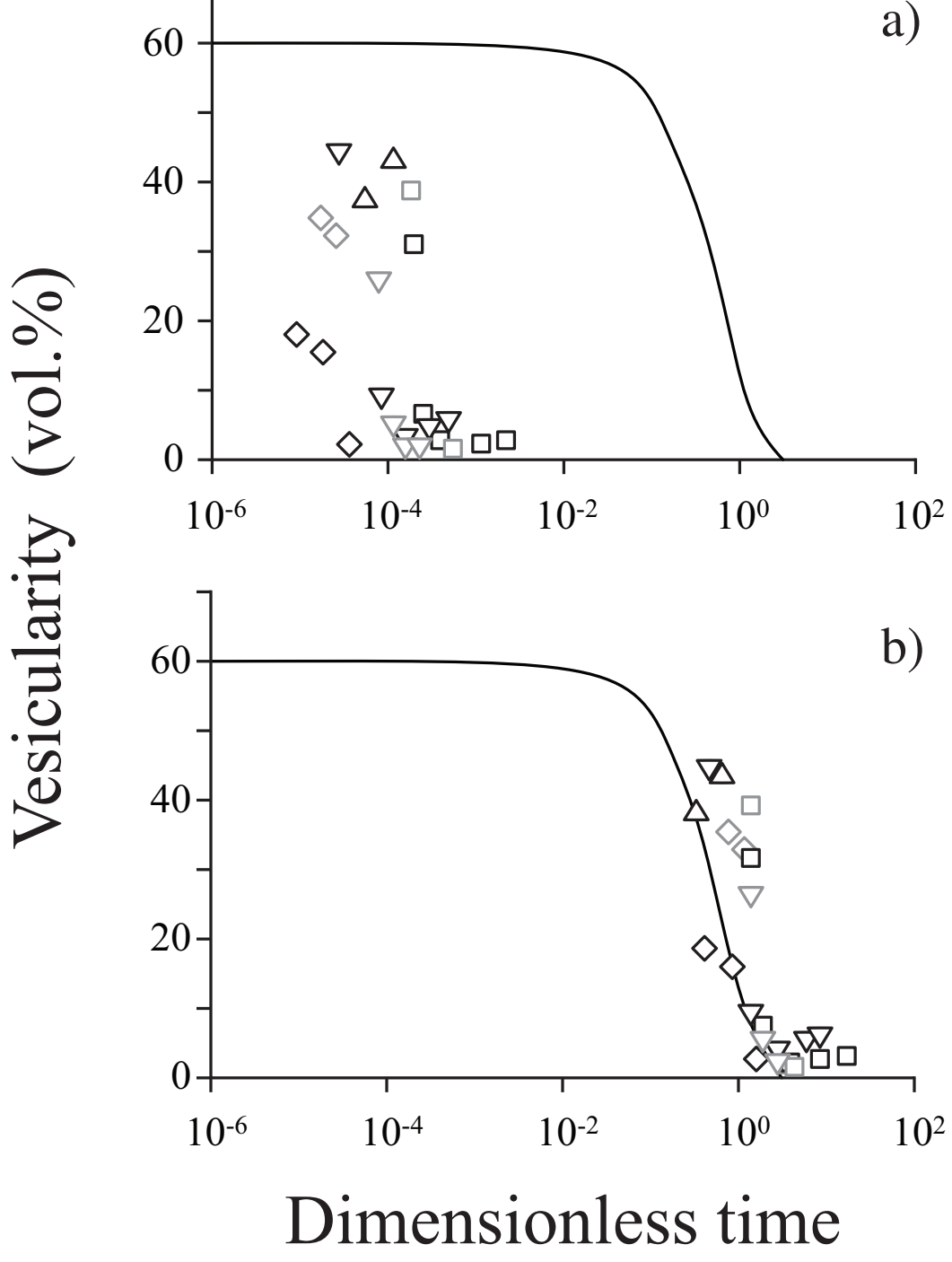


Figure 8

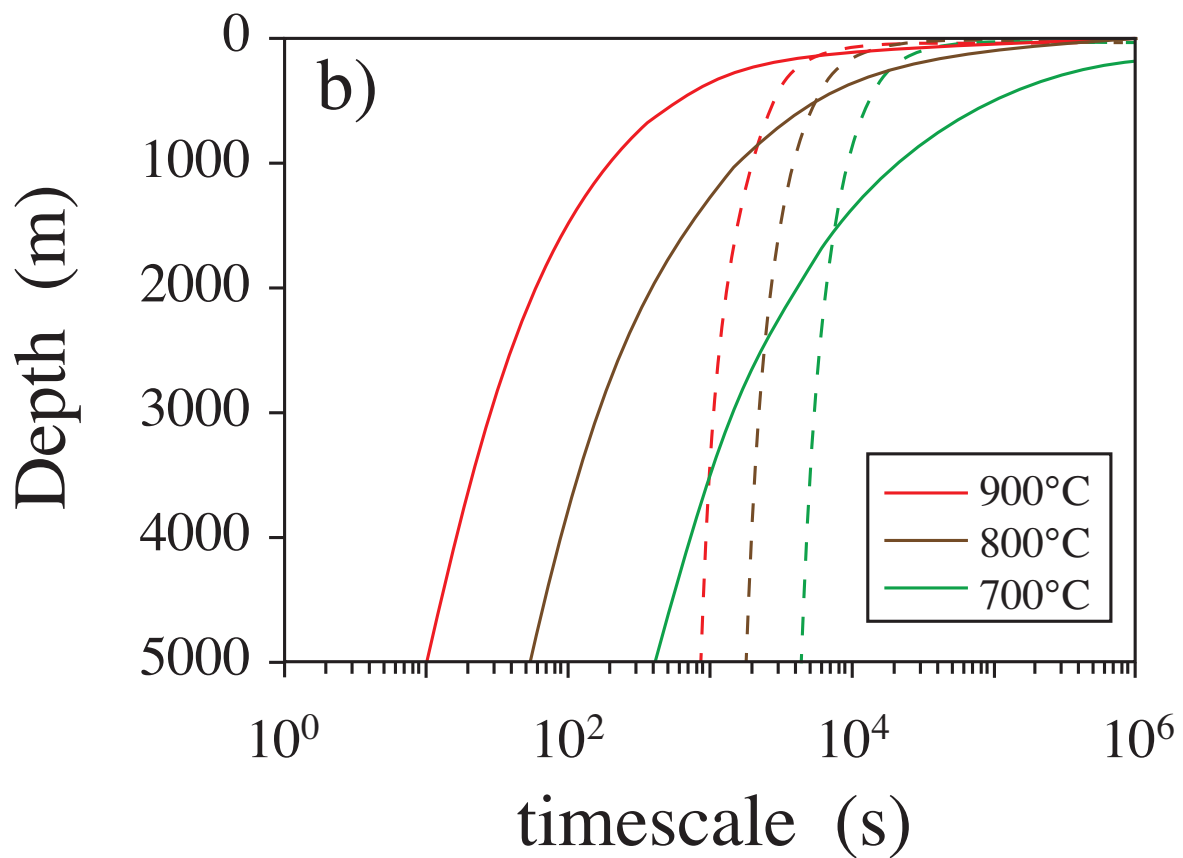
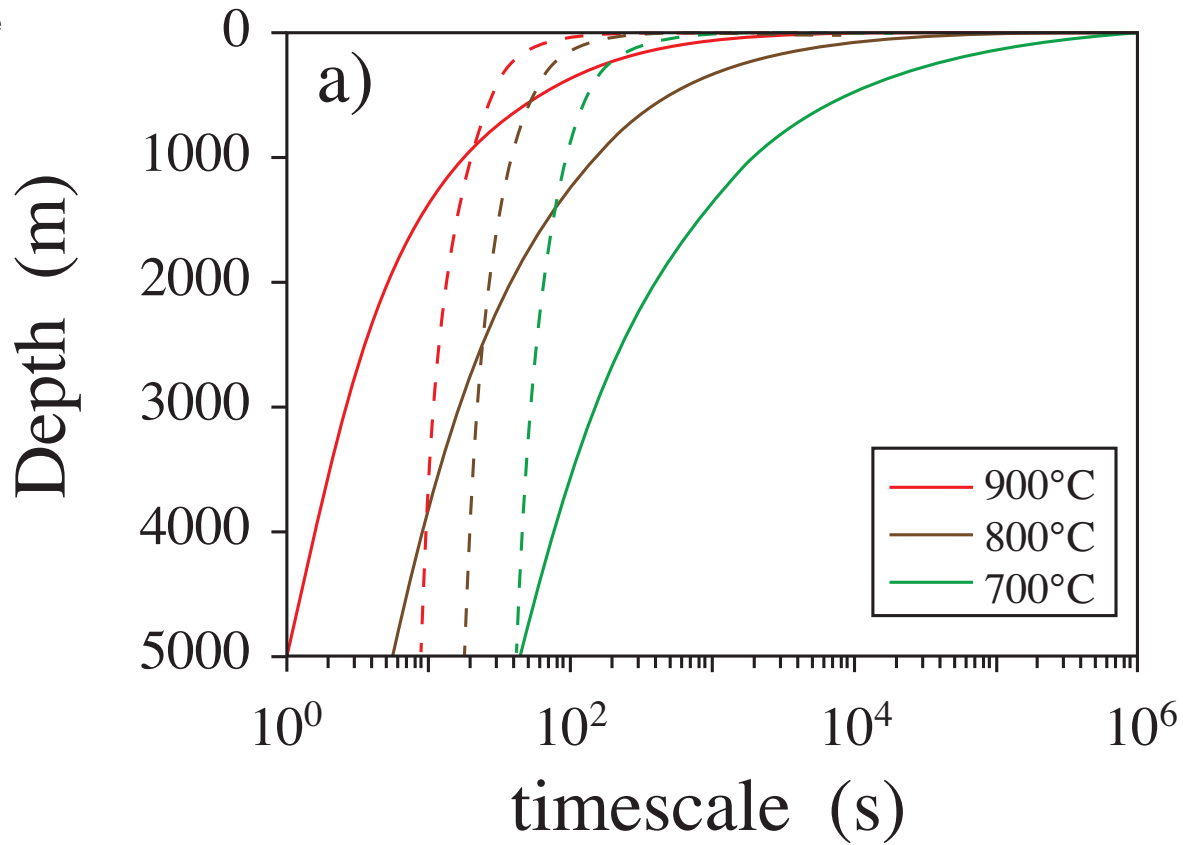


Figure 9

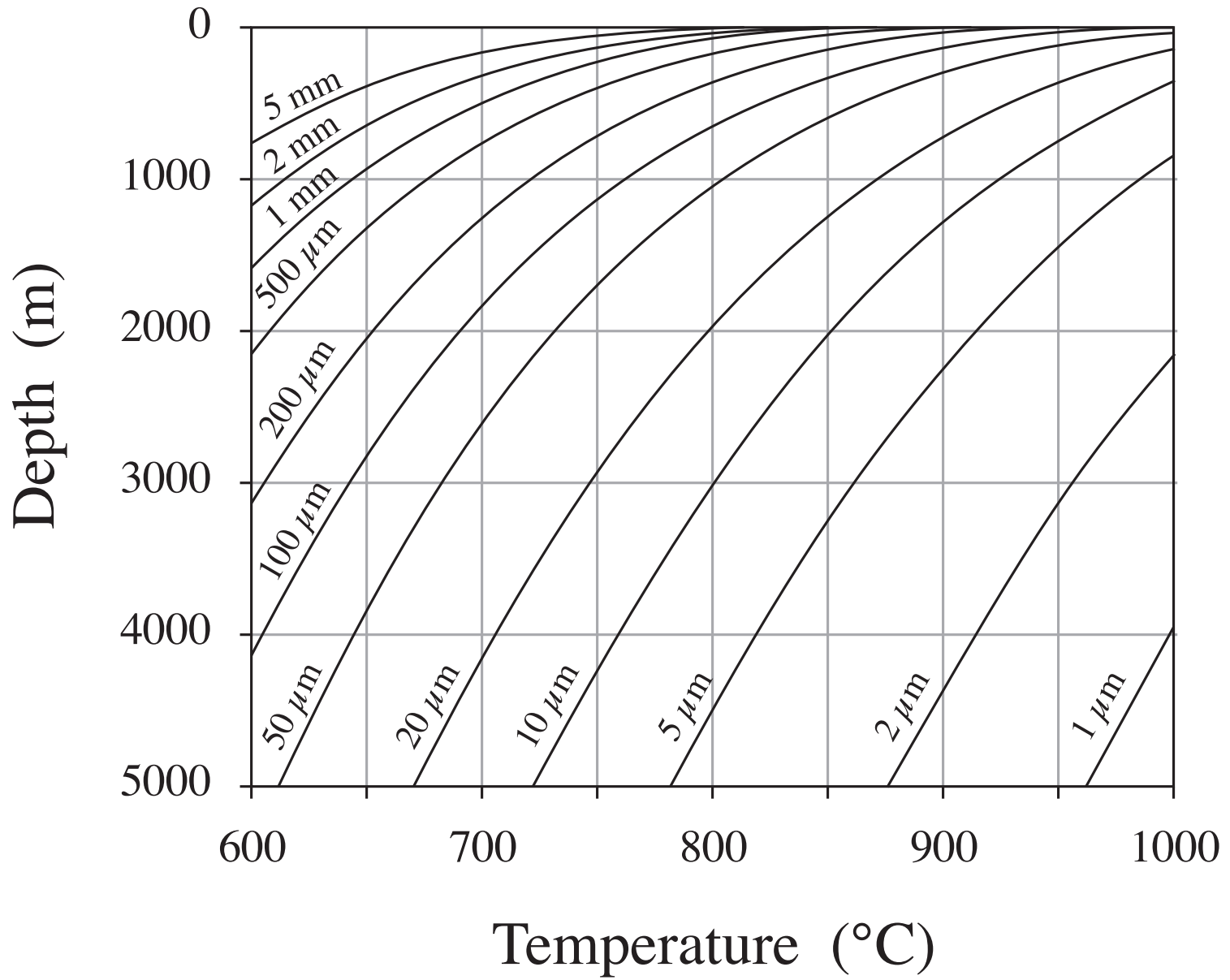


Figure 10

**Table 1: Experimental Run Conditions and Results**

Run	T <sup>a</sup> (°C)	P <sup>a</sup> (MPa)	t <sup>a</sup> (min)	$\phi^b$ (vol.%)	$N_v^{(s)c}$ (cm <sup>-3</sup> )	$N_v^{(c)c}$ (cm <sup>-3</sup> )	Size <sup>d</sup> ( $\mu$ m)	H <sub>2</sub> O <sup>e</sup> (wt.%)	Fi <sup>f</sup>
Unsieved powder as starting material									
G-1653	700	40	5	–	–	–	–	–	0.2
G-1664	700	40	15	18.3	–	–	–	2.26±0.25	0.7
G-1650	700	40	30	15.7	–	–	–	–	1.4
G-1652	700	40	60	2.4	10 <sup>6.69</sup>	10 <sup>6.25</sup>	7±8	–	2.9
G-1657	725	20	5	–	–	–	–	–	0.2
G-1655	725	20	15	–	–	–	–	–	0.6
G-1654	725	20	30	38.1	–	–	–	–	1.3
G-1656	725	20	60	43.6	–	–	–	–	2.6
G-1647	750	40	5	44.2	–	–	–	1.86±0.25	0.4
G-1658	750	40	15	8.7	10 <sup>6.06</sup>	10 <sup>5.53</sup>	5±5	–	1.1
G-1651	750	40	20	4.7	10 <sup>6.38</sup>	10 <sup>6.02</sup>	6±4	2.63±0.07	1.5
G-1646	750	40	30	3.6	10 <sup>6.49</sup>	10 <sup>5.55</sup>	8±6	–	2.3
G-1648	750	40	60	5.1	10 <sup>6.54</sup>	10 <sup>4.73</sup>	18±17	–	4.5
G-1660	750	40	90	5.5	10 <sup>6.91</sup>	–	16±12	–	6.8
G-1642	800	40	5	31.4	–	–	–	–	0.6
G-1659	800	40	7	7.0	10 <sup>6.69</sup>	10 <sup>6.14</sup>	7±5	2.36±0.11	0.8
G-1649	800	40	10	2.8	10 <sup>6.55</sup>	10 <sup>5.98</sup>	9±7	2.53±0.09	1.1
G-1640	800	40	30	2.4	10 <sup>6.72</sup>	–	10±16	–	3.4
G-1641	800	40	60	2.9	10 <sup>6.46</sup>	–	13±12	–	6.8
Sieved powder as starting material									
G-1668	700	40	60	35.2	–	–	–	–	0.7
G-1669	700	40	90	32.7	–	–	–	–	1.0
G-1643	750	40	30	25.9	–	–	–	2.45±0.16	0.5
G-1667	750	40	45	5.1	10 <sup>5.47</sup>	10 <sup>5.04</sup>	13±12	–	0.8
G-1661	750	40	60	1.5	10 <sup>5.67</sup>	10 <sup>5.07</sup>	17±15	–	1.0
G-1663	750	40	90	1.9	10 <sup>5.86</sup>	10 <sup>5.20</sup>	19±13	–	1.6
G-1666	800	40	10	38.8	–	–	–	–	0.3
G-1662	800	40	30	2.0	10 <sup>5.46</sup>	10 <sup>4.75</sup>	20±16	–	0.8

<sup>a</sup>temperature (in °C), pressure (in MPa), and time (in minutes) of the experiment.

<sup>b</sup>vescularity (in vol.%) of the experiment, includes all vesicle types.

<sup>c</sup>number density (in numbers per cm<sup>3</sup>) of spherical (s) or contorted (c) vesicles.

<sup>d</sup>average diameter (in  $\mu$ m) of 50 to 200 spherical vesicles.

<sup>e</sup>average dissolved H<sub>2</sub>O contents (in wt.%) with  $\pm 1$ s errors listed.

<sup>f</sup>dimensionless Fick number calculated from Eqn. 3, assuming solubility concentrations for H<sub>2</sub>O.